2015

Fault-related fold kinematics recorded by terrestrial growth strata, Sant Llorenç de Morunys, Pyrenees Mountains, NE Spain

James Carrigan
Lehigh University

Fault-related fold kinematics recorded by terrestrial growth strata, Sant Llorenç de Morunys, Pyrenees Mountains, NE Spain

By

James Carrigan

A Thesis

Presented to the Graduate and Research Committee

of Lehigh University

in Candidacy for the Degree of

Masters of Science

in

Earth and Environmental Sciences Department

Lehigh University

November 16, 2015

Thesis is accepted and approved in partial fulfillment of the requirements for the Masters of Science in Department of Earth and Environmental Sciences.

Fault-related fold kinematics recorded by terrestrial growth strata, Sant Llorenç de Morunys, Pyrenees Mountains, NE Spain

James Carrigan

_____

Date Approved

_____

Professor David J. Anastasio

Thesis Advisor
Chair, Earth and Environmental Sciences Department

_____

Professor. Kenneth P. Kodama

Committee Member
Earth and Environmental Sciences Department

_____

Dr. Josep M. Parés

External Committee Member
Centro National de Investigación sobre la Evolución Humana, Burgos, Spain

Acknowledgments

This manuscript would not have been made possible with out the assistance of all those who contributed and dedicated their time to improving it. Some specific people I would like to thank include: my advisor Dave Anastasio for providing constant feedback throughout the process and helping me to focus on the significance and process as opposed to setting; committee member Dr. Josep M. Parés for his contributions with the magnetostratigraphy aspect of this work as well as his helpful field assistance; committee member Proessor Ken Kodama and graduate student Daniel Minguez (PhD 2014) for their support with paleomagnetic and cyclostratigraphic methods; Lehigh undergraduate Marisa Repasch (BS 2013) for sample collection fall 2013 and AMS analysis; Claudia Alvárez (PhD 2015), University of Burgos, for field assistance in the summer of 2014; and Josep Cases, from Sant Llorenç de Morunys for his excellent help.

Partial funding for this project was provided to James Carrigan from the AAPG L. Austin Weeks Memorial Grant and the Earth and Environmental Science Department Palmer Research Fund, Lehigh University.

Table of Contents

Page

List of Figures

Page

Figures

Appendix Figures

List of Tables

Abstract

This study develops a high-resolution chronostratigraphy age model based on magnetic susceptibility (χ) variations to determine folding rates recorded by Eocene-Oligocene synorogenic terrestrial growth strata of the Berga Conglomerate Formation near Sant Llorenç de Morunys, NE Spain. This region was selected for its excellent preservation and exposure of synorogenic growth strata which allows for examination of deformation at high-resolution (20 kyr) time scales. The Berga Conglomerate was sampled for rock magnetic, paleomagnetic, and χ cyclostratigraphy analyses. Analysis of rock magnetic measurements indicate paramagnetic phyllosilicates are the dominant minerals that control χ cyclostratigraphy in a mixed mineral assemblage. Anisotropy of magnetic susceptibility (AMS) fabrics are most consistent with a fixed hinge flexural folding and transecting cleavage developed in the foreland synclinal hinge. Paleomagnetic reversal stratigraphy provided absolute time frame on folding at the million year timescale. Time series analysis of χ variations shows statistically significant power in expected orbital ratios (long eccentricity, obliquity, and precession). A calibrated age model was constructed using χ variations tuned to obliquity (41 kyr) cycles, which focuses power into precession index bands and long eccentricity. The age model predicts the onset of deformation at 33.85 Myr and shows that deformation and sediment accumulation rates were unsteady at 20 kyr time scales. Deformation rates range from quiescent to 100°/Ma and are not related to changes in sediment accumulation rate. Modeled fault slip predicts variable displacement rates ranging from 115 - 265 m/Myr.

1 Introduction

In this study I seek to combine kinematic constraints and high resolution timing to recover orogenic fold evolution at 10^4 - 10^5 yr timescales. Terrestrial deposits in foreland basins provide the best record of the sediment from nearby tectonically active regions and are ideal for recovering fault slip at intermediate timescales. The Sant Llorenç structure was selected because of the excellent exposure of syntectonic structures and because of the well preserved growth strata due to close proximity to the sediment source. Because growth strata record both the interaction between fold evolution and changes in depositional environment (Figure 1) separation of orogenic and sedimentary processes is important to tectonic interpretations. An obstacle to terrestrial systems is that they are typically devoid of robust chronologic control which makes high resolution timing of fault slip difficult. Terrestrial deposition occurs in high energy systems, oxidizing environments, and with large depositional hiatus, all of which make preservation of chronologic markers unlikely. Terrestrial fluvial environments are suggested by Jarolmack and Paola [2010] to shred high frequency signal making cyclostratigraphic timing difficult. However, Milankovitch scale frequencies occur on long timescales and should be preserved in the sedimentary record. Rock magnetic clycostratigraphy provides a robust method to date growth strata which can be used to constrain slip of buried faults.

Rock magnetic properties have been used as a method for providing a high-resolution chronostratigraphy in many systems [Latta et al., 2006; Kodama and Hinnov, 2014]. Cyclostratigraphy has been shown to provide temporal resolution on the order of $10^4 - 10^5$ years in marine settings [Gunderson et al., 2014; Latta et al., 2006; Hinnov et al., 2013; Kodama et al., 2010] and in young fluvial

sediments [Nádor et al., 2003]. Terrestrial foreland basins may be ideal sites for cyclostratigraphy as they have sufficiently high sediment accumulation rates to recover high frequency orbital signals. Absolute time was determined by correlating our study sites with the global magnetic reversal chronology of Gradstein *et al.* [2012]. Absolute time allows for calibration of a cyclostratigraphic section to Earth's known orbital parameters.

In order to determine kinematic control on fault-related folding, oriented cores were analyzed using anisotropy of magnetic susceptibility (AMS). The kinematics of the Sant Llorenç structure were debated [Alonso et al., 2011; Ford et al., 1997; Suppe et al., 1997] but never definitively resolved. Past studies were based on growth strata geometries and meso-scale fabrics, which were unable to constrain the movement of the fold hinge through time. AMS was used to constrain fold kinematics and allowed for a robust fold modeling to occur. Combining kinematic constraints and high resolution timing allows for a detailed model of fold evolution through time.

2 Geologic Setting

This study focuses on the proximal foreland basin between the Ebro Basin and the Spanish Pyrenees in northeastern Spain (Figure 2). The Pyrenean mountain front is typical of terrestrial orogens with multiple thrust faults and folds such as the Vallfogona thrust. Displacement of the Vallfogona thrust sheet created extensive syntectonic folding of the footwall during shortening [Puigfàbergas et al., 1992] causing a large structural basin. Footwall deposits record the typical orogenic sequence of marine to terrestrial deposition as the Vallfogona breached the surface [Puigfàbergas et al., 1992; Williams et al., 1998]. This study will be focused on

the fluvial sediments influenced by this deformation. Previous studies *e.g.* [Riba, 1976; Ford et al., 1997; Suppe et al., 1997; Abdul Aziz et al., 2000] have approached these processes at a lower time scale resolution. A few studies around the region also explore the sedimentology of these syntectonic deposits [Williams et al., 1998; Barrier et al., 2010] or seperate nearby basins [Barberá et al., 2001; Costa et al., 2010; Mochales et al., 2012].

2.1 Berga Conglomerate Formation

Stratigraphy

Originally proposed by Solé-Sugrañes [1970; 1972], the Berga Conglomerate Formation was described in detail by Riba [1976] along the Cardoner River, the main N-S drainage in the study area. Just north of the town of Sant Llorenç de Morunys, the Berga Conglomerate lies conformably on the marine marls and marly limestones assigned to the Bartonian-Lower Priabonian ([Solé-Sugrañes and Mascareñas, 1970]), which are laterally equivalent to the Igualada Formation further south within the Ebro Foreland Basin. The Berga Conglomerate Fm. consists of conglomerates, sandstones and siltstones of alluvial and fluvial origins. For the purpose of this study I have divided the Berga Conglomerate into seven formations which generally follow the naming conventions found in Ford *et al.* [1997] and Willams *et al.* [1998]. A comparison between formations used in this study and previous studies can be found in the Appendix Figure 1. Formation descriptions for this study are based on 1) presence of conglomerate, 2) bed thickness, and 3) facies association. In this study the Camps de Val Llonga Formation consists of predominantly sand and siltstones with occasional conglomerates not exceeding 50 m in maximium thickness. The El Castell Formation is characterized by two

massive, >75 m, conglomerate beds separated by a small amount of sand and siltstones. Other formations of the scheme of Ford *et al.* [1997] are used in this study without modification.

The Berga Conglomerate Fm. [Riba, 1976] is composed of proximal alluvial fans and fluvial systems that are transporting the sediment formed in orogensis to the Ebro Basin [Riba, 1976; Williams et al., 1998; Vergés et al., 2002; Barrier et al., 2010] (Figure 1). Changes in drainage area, drainage location, and tectonic rates all influence the sedimentary depositional environment through time. A stratigraphic column presented in Figure 4 illustrates how the depositional environment has changed and is recorded in changes in litho-facies.

2.2 Previous Structural Interpretations

The kinematics of the Sant Llorenç structure was studied as early as the 1960's by Riba [1967]; however, most of the literature followed the publication of Riba's expanded study [Riba, 1976]. There were three different controlling mechanisms proposed for the formation of the Sant Llorenç structure: fold limb rotation [Ford et al., 1997], kink-band migration [Suppe et al., 1997], and a hybrid monclinic folding model with both limb rotation and hinge migration [Alonso et al., 2011]. Despite the differences between the folding mechanisms, all prior work suggests that the folding is related to the propagation of a blind thrust driven by the Pyrenean Orogeny. Our study seeks to examine which, if any, of these proposed folding mechanisms satisfy the kinematic data.

3 Methods

Specimens were collected for this study during three field seasons: October 2013, May 2014, and May 2015 and data from earlier field work influenced later collection strategies. Samples are classified as either oriented or unoriented based on whether or not an *in situ* orientation was needed for analysis. All samples have nearby bedding orientations and lithologic descriptions recorded.

3.1 Magnetic Mineralogy

Unoriented samples were processed to determine the magnetic mineralogy of the Berga Conglomerate Fm. Samples were used to identify (1) ratio of goethite to goethite + hematite (G/(G+H)) as a proxy for moisture conditions during sediment deposition [Kämp and Schwertmann, 1983; Yapp, 2001; Sangode and Bloemendal, 2004] based on thermal demagnetization of isothermal remanent magnetization (IRM) modified from Lowrie [1990], (2) relative contributions to magnetic remanence of different coercivity phases based on IRM acquisition modeling [Kruiver et al., 2001], and (3) relative influence of paramagnetic minerals in χ based cyclostratigraphy by room and low temperature susceptibility analysis.

200 specimens had IRMs applied in an ASC Scientific IM-10-30 impulse magnetizer in two steps to determine magnetic mineralogy. A field of 0.1 T was applied along the x axis and was measured in a 2G Enterprises, Inc. 755R superconducting magnetometer. Then a 5 T field was applied in along the x axis to overprint the first IRM and the sample was remeasured. Samples were then thermally demagnetized at 125 °C and measured again. Thermal demagnetization was performed in an ASC Scientific TD-48 thermal specimen demagnetizer.

Seven samples, chosen for variations in grain size and coloration, underwent detailed IRM acquisition in the IM-10-30 impulse magnetizer. Each sample was crushed and sieved with grains less than 2.5ϕ used for analysis. All samples were placed in a field free room for at least a week to reduce any field obtained during processing and had not been exposed to any strong magentic field previously. IRMs were applied in 23 steps which were chosen to be as close as possible to uniform in log spacing. The coercivity components were modeled following Kruiver *et al.*'s [2001] software.

Room and low temperature bulk susceptibility was conducted for 10 additional specimens to determine the relative influence of paramagnetic, diamagnetic, and ferromagnetic minerals. Sample χ were measured at room temperature (21 °C) using a KLY-3S Agico susceptibility meter. Specimens were then immersed in liquid nitrogen for 2 minutes to fully cool the sample to -196 °C and were quickly removed and measured in the KLY-3S meter.

3.2 Oriented Sampling Strategy

Oriented cores were collected for paleomagnetic reversal stratigraphy and anisotropy of magnetic susceptibility (AMS) analyses. Samples were collected using a water cooled drill, nonmagnetic 1" drill bits, and orienting equipment. All sites had $\geq$3 cores and >5 specimens in order to ensure statistical significance of our results [Fisher, 1953].

Magnetic Reversal Stratigraphy

Samples were collected for the magnetic reversal stratigraphy during each field season and sample spacing was refined after a preliminary magnetostratigraphy

was constructed. Preliminary results suggested a minimum polarity interval of 290 kyr and an average deposition rate of 0.25 m/kyr. Therefore, a sampling interval of 15 m was selected to allow for multiple consecutive sites in the shortest interval while maintaining enough spacing to make >1.5 km sampling feasible. In total, 119 sites were analysed with a least 3 oriented cores per site allowing Fisher [1953] means to be calculated.

Paleomagnetic measurements were made on a 2G Enterprises 755R superconducting rock magnetometer at CENIEH, Burgos, Spain. Thermal demagnetization was conducted with a ASC Thermal Demagnetizer in up to 15 temperature steps from 150°C to 660°C. Alternating field demagnetization was used on a small number of samples using an in-line 2G 600 AF sample demagnetizer. Characteristic Remanence Magnetizations (ChRM) were completed for all specimens using principal component analysis [Kischvink, 1980]. Vitural Geomagnetic Pole (VGP) latitudes were used to determine local magnetostratigraphy.

Anisotropy of Magnetic Susceptibility (AMS)

AMS samples were used as a proxy for strain to establish fold kinematics. Samples for AMS analysis were collected from all structural positions the steeply overturned limb of the fold, the hinge of the fold, and the upright shallowly dipping limb of the fold. Cores were analyzed in a KLY-3S Agico susceptibility meter at Lehigh University, to determine their degree of anisotropy. This analysis consists of measurements in 15 different orientations to construct an anisotropy tensor. Using this method provides the three principal axes of susceptibility, $\kappa 1$, $\kappa 2$ and $\kappa 3$; the degree of anisotropy, P' [Jelinek, 1981] given by:

$$P' = e\sqrt{2[(\eta_1 - \bar{\eta})^2 + (\eta_2 - \bar{\eta})^2 + (\eta_3 - \bar{\eta})^2]}$$

and the shape factor, T [Jelinek, 1981] given by:

$$T = \frac{(2\eta_2 - \eta_1 - \eta_3)}{(\eta_1 - \eta_3)}$$

Where $\eta_1 = \ln(\kappa 1)$; $\eta_2 = \ln(\kappa 2)$; $\eta_3 = \ln(\kappa 3)$; and $\bar{\eta} = (\eta_1 + \eta_2 + \eta_3)/3$. Methods used in this study are based on Tarling and Hrouda [1993].

3.3 Unoriented Sampling Strategy

Pilot data were collected at 50 cm intervals before an average sediment accumulation rate was determined from preliminary magnetic reversal stratigraphy. Later field season sampling strategies had 75 cm and 100 cm sample intervals to ensure the 4-5 kyr spacing needed for precessional index resolution. A few samples were drilled using a carbide tipped drill bit, but this method proved to be time consuming and unwieldy; small hand samples were collected for >90% of the specimens collected. All hand samples were crushed and sieved to <2.5 ϕ used for analysis and care is taken to prevent any crushing of obvious clasts. For conglomerate beds matrix-rich sample sites were chosen to limit clast contamination. The crushed sediment was packed into pre-weighed 8 cm^3 nonmagnetic containers and solidified with sodium silicate to prevent movement of sediment during analysis.

Rock Magnetic Cyclostratigraphy

The rock magnetic data span 800 m from pregrowth strata at the base to the top of the section (Figure 4). Processed unoriented samples underwent two seperate magnetic analyses χ and anhysteretic remanent magnetization (ARM) at Lehigh University. These methods were chosen because of success of studies using both susceptibility [Gunderson et al., 2013; Kodama et al., 2010; Rafini and Mercier,

2002] and ARM [Latta et al., 2006; Hinnov et al., 2013] as a proxy for climate variation. All ARM methods, results and discussion are located in the appendixes.

Low field χ was measured using a KLY-3S Kappabridge and mass normalized. Magnetic susceptibility is controlled by ferromagnetic, paramagnetic, and diamagnetic minerals. In terrestrial sediments, paramagnetic grains such as clay particles very often dominant the total χ signal [Parés and van der Pluijm, 2002]. Data from both χ and ARM was then processed and analyzed following the same procedure. Any statistical outliers $> 5\ \sigma$ from the mean were discarded. Due to the high amplitude variability of both datasets I applied a $\log_{10}$ normalization of the data to decrease this variability. Gaps larger than 5 m were filled using single spectrum analysis (SSA) utilizing the SSA-MTM toolkit [Ghil et al., 2002; Kondrashov and Ghil, 2007] to eliminate gap artifacts. SSA results fill gaps in data by using dominant frequencies in the data itself so it is an useful way to fill sampling gaps without introducing artifical cycles to the dataset. The SSA period chosen to fill gaps was to provide the best fit to the data while retaining multilevel frequencies. In total, 13 % of the χ data is from SSA gap filling. After all the gaps were filled the data series was resampled at equal intervals using a linear interpolation every 15 cm .

The data series were analyzed using the multi-taper method (MTM) [Thomson, 1982] spectral analysis with 2π prolate multitapers to identify significant periodicities. The data series were tied to absolute time using the magnetic reversal chronology correlated to chron boundary ages obtained from Gradstein *e*t al. [2012] using the astrochron package for R [Meyers, 2014; Meyers et al., 2001]. After the data series was correlated to absolute time it was equally resampled every 1 kyr. Power spectra were produced for a un-tuned data series using the SSA-MTM toolkit [Ghil et al., 2002]. I identified significant frequencies in the power spectra

at the 90%, 95%, 99% confidence interval above a robust red noise model following Mann and Lees [1996]. After Milankovitch-scale frequencies were observed in the data a detailed cyclostratigraphy was constructed by tuning the Gaussian filtered timeseries to the theoretical obliquity signal (41 kyr) [Laskar et al., 2004] in the χ data series.

4 Results

4.1 Magnetic Mineralogy

A representative model of IRM acquisition for sample BUSA-146 is shown as Figure 5. All the samples show either two or three magnetic components. One component has a low coercivity (30 mT) and two high coercivity components are also identified around 1 T and >3 T, but are poorly determined. The low coercivity component ranges from 10 mT to 60 mT and becomes saturated around 300 mT. The intermediate coercivity component ranges from 631 mT to 1584.9 mT and averages around 1000 mT; this component is fully saturated. The highest coercivity component ranges from 3162.3 mT to 5011.9 mT and is not fully saturated by our method. All three ferromagnetic components contribute to the χ cyclostratigraphy.

Results from IRMs applied to the 200 samples were assigned to three mineralogies: magnetite, 0.1 T measurement; hematite, 125 °C - 0.1 T measurement; and goethite, 5 T - 0.1 T measurement. This division is based on the relative coercivity of each magnetic mineral, goethite's low 120 °C unblocking temperature, and coercivity analysis of seven separate samples support a three component mineralogy. The magnetite component has an average value of $8.81*10^{-6}$ Am^2/kg and ranges

from 8.34 *10^{-7} to 1.37*10^{-4} Am^2/kg. The hematite component has an average value of 2.02*10^{-4} Am^2/kg and ranges from 1.84 *10^{-5} to 6.65*10^{-4} Am^2/kg. The goethite component has an average value of 2.05*10^{-4} Am^2/kg and ranges from 3.34 *10^{-5} to 5.95*10^{-4} Am^2/kg. G / (G + H) was calculated for each sample and ranges from 0.107 to 0.931 (Appendix Figure 2).

Results of low temperature susceptibility are graphed in Figure 6 and displayed in Table 1. All samples showed an increase in susceptibility at lower temperatures between 200-400 %. In order to determine the relative strength of magnetite to paramagnetic minerals in bulk susceptibility measurements calculations following Parés [2004] were conducted. The average satuaration magnetic moment for this study is 6.7 x 10^{-8} A/m which suggests a magnetite concentration of 0.4 x 10^{-4} % assuming a magnetite grain size of 1 μm [O'Reilly, 1984]. This corresponds to a volume susceptibility of 2 x 10^{-6} or $\ll$ 1 % of the average bulk susceptibility of the samples in this study. Therefore, ferromagnetic minerals identified through IRM acquisition modeling had a small contribution to the low field susceptibility measurements.

4.2 Magnetic Reversal Stratigraphy

Thermal demagnetization isolated sample ChRMs better than alternating field method and was selected for most of the samples. Most specimens show an over-print, often parallel to the field direction (Figure 7A) Thermal demagnetization was applied until intensities were too low when and remanence became erratic due to spontaneous mangetization. Typically, ChRM directions were obtained between 300-400 °C. After calculating ChRM for individual specimens, site mean directions were computed and the corresponding VGP latitudes used to establish

the local magnetostratigraphy of the Berga Conglomerate Fm.

Data was classified into two groups based on angular distance from expected normal polarity paleopole or its antipode. VGP latitudes $< 45^{\circ}$ of expected value are designated normal or reversed respectively. VGP latitudes in $> 45^{\circ}$ of expected value are indeterminate in nature. Two or more consecutive sites of the same polarity constitute a magnetozone in the local magnetostratigraphy; however, one site with a different polarity than its neighbors is designated a submagnetozone. Following this, ten magnetozones were identified, N1-N5, R1-R4, and I1. The border between magnetozones was chosen as the mid point between any two opposite polarities or 15 m from the first sample when entering or exiting an indeterminate region.

ChRm directions were compared before and after bedding correction (Figure 7B). In geographic coordinates (*i.e.* before bedding correction), two clusters are observed: south and downwards and north and upwards respectively. After bedding correction, directions are oriented north and down or south and upwards, displaying both normal and reverse polarities respectively. There is a considerable scatter in directions which is probably due to (1) incomplete removal of the secondary component, and (2) coarse grain size of the majority of sampled horizons.

4.3 Anisotropy of Magnetic Susceptibility (AMS)

Table 1 shows the main parameters obtained from AMS measurements. The location of AMS sites are shown in map view (Figure 2). All samples show low levels of anisotropy, varying $\pm 3\%$ from the intermediate axis, but the shape anisotropy varies with structural location. Ellipticity for hinge sites is oblate, while limb sites display nearly equant anisotropy. The low level of anisotropy observed in the

dataset is pervasive and extends from north to south for >10 km. Orientation analysis of the three principal axes of susceptibility were constructed for each region to better understand the geometry of the strain (Figure 8). Both limbs show $\kappa 1$, the maximum susceptibility axis, is oriented parallel to the strike of bedding, $\kappa 2$, the intermediate susceptibility axis, is in the bedding plane oriented nearly N-S, and $\kappa 3$, the minimum susceptibility axis, is orthogonal to the bedding plane. The overturned limb shows $\kappa 3$ rotated clockwise from cleavage The hinge shows $\kappa 1$ oriented parallel to the strike of bedding and the $\kappa 2$ & $\kappa 3$ axes produce a girdle oriented nearly N-S. Hinge specimens show a strong cleavage in fine grained lithologies (Figure 9). In sites displaying cleavage, $\kappa 1$ is oriented parallel to the strike of the foliation, which is the same as the strike of bedding.

4.4 Rock Magnetic Cyclostratigraphy

Bulk suceptibility values range from 3.29×10^{-12} to 1.56×10^{-9} m^3/kg and shows multi-hierarchical amplitude and frequency variability throughout the data series (Figure 10). Amplitude variations in χ are most likely related to changes in lithology. High amplitude variations coincide with conglomerate facies especially in the most poorly stratified conglomerates. Low variations in amplitude is recovered from the sandy and silty intervals. Frequency variations range from 2 - 100 m and relate to lithologic variability. Short scale frequency variations occur on the same scale as sand and silt fluvial overbank and channel packages while long scale variations relate to alluvial to fluvial sequences. Power spectra obtained from MTM spectral analysis shows significant power in frequencies associated with Milankovitch cycles. Specifically the precession index band and obliquity (41kyr) are significant to the 99% confidence level from the robust red noise model [Mann and Lees, 1996].

To reduce the effects of high frequency variable sedimentation rates on stratigraphic ages the χ data series was then correlated to the theoretical obliquity model of Laskar *et* al. [2004]. This was accomplished by applying a Gaussian filter centered on 1/41 kyr (with cutoffs of $\pm$1/5 kyr) to the data series. The filtered data series was then correlated to the orbital obliquity model [Laskar et al., 2004] by matching visually identified maxima of the filtered series to maxima of the theoretical model [Laskar et al., 2004]. The tuned data series shows similar significant frequencies as the un-tuned and decreases non-Milankovitch cycles (Figure 12) suggesting that signals recovered from χ data are global orbital variations. The significant peak at 20 kyr will be used to provide high resolution timing for the structural modeling.

5 Discussion

5.1 Magnetic Mineralogy

IRM acquistion modeling suggests multiple ferromagnetic minerals are present in Berga Conglomerate Fm. samples. These are interpreted to be magnetite for the low coercivity phase at around 30 mT. This phase is similar to biogenic soft magnetosomes produced in anoxic lakes (40 mT) [Egli, 2003]; however, it is more likely that this is a detrital inorganic magnetite. The Berga Conglomerate was deposited in fluvial to alluvial systems making biogenic magnetite unlikely. The higher coercivity components are consistent with the coercivities of hematite and goethite. Thermal demagnetization supports this assumption with a loss of remanence around 120°C and another high temperature $>$ 650 °C component (Figure 7b).

G / (G + H) values show multilevel frequency variations (Appendix Figure 2) with a majority of samples within 0.4 - 0.6. Lower values of G / (G + H) are indicative of drier/warmer conditions and higher values indicate higher precipitation [Yapp, 2001; Harris and Mix, 2002; Abrajevitch et al., 2009]. G / (G + H) also records long term shifts in depositional environment. From 850-880 m the G / (G + H) ratio shows a shift from drier to wetter environment possibly related to the onset of deformation at 825 m. After 890 m G / (G + H) ratios stabilize around the new average value of 0.5. A change in climate to wetter conditions recovered from the G / (G + H) ratio likely influences the formation of paramagnetic clays as the product of weathering source material. Therefore, a change in local climate during deformation likely contributed to an increase in paramagnetic clay formation that is recovered in χ measurements.

While χ would recover ferromagnetic, paramagnetic, and diamagnetic signals low temperature analysis suggests that paramagnetic contributions are large in comparison to the ferromagnetic contribution in susceptibility. Susceptibility of paramagnetic minerals such as phyllosilicates show an inverse temperature relationship [Richter and van der Pluijm, 1994; Parés and van der Pluijm, 2002] following the Curie-Weiss Law:

$$\chi = \frac{C}{T - T_C} \tag{1}$$

Substituting typical values [Beausoleil et al., 1983] for these parameters, C = 5-17 x 10^{-6} $\frac{m^3 K}{kg}$; T = 77 K (liquid nitrogen); and $T_C \approx 0$ K, gives a 3.8 times increase in susceptibility as compared to room temperature (300 K). Ferromagnetic minerals do not show a temperature dependence so a large increase in susceptibility at low temperatures is indicative of high concentrations of paramagnetic minerals

[Parés et al., 1999; Tauxe, 2010]. Diamagnetic contributions must also be relatively small as all specimens display a positive response to the applied field.

5.2 Magnetic Reversal Stratigraphy

Just north of the studied section, the Berga Fm. lies conformably on marine marls and marly limestones of which are laterally equivalent to the Igualada Formation. The Igualada Fm. and its lateral equivalences have been profusely studied by a number of authors ([Taberner et al., 1999; Costa et al., 2010; Rodríguez-Pintó et al., 2012]), and is shown to have a Bartonian age (middle-upper Eocene) [Solé-Sugrañes and Mascareñas, 1970; Puigfàbergas et al., 1992], or chron C17. Our local magnetic polarity stratigraphy begins with a rather long normal polarity chron (N1) and shows a conspicuous long reverse chron (R4) in the mid-upper part. The GPTS ([Gradstein et al., 2012]) shows that after chron C17 (middle-late Eocene), the *post quem* of the Berga Fm., the first prominent reverse chron appears to be C13r, which is followed by an even longer reverse chron (C12r). The most reasonable interpretation is that normal magnetozone N4 corresponds to Chron C13n, rendering the assignment of magnetozones R2/R3 and R4 as Chrons C13r and C12r respectively. Continuing the one-to-one correlation downward of magnetozones to chrons, normal magnetozones N3 and N1 would correspond to Chrons C15n and C16n respectively. The overall local magnetostratigraphy would then encompass Chrons C16n to C12n, rendering the age of the Berga Fm. Late Eocene-Early Oligocene (ca. 36 to 31 Ma).

Marine marls (equivalent to the Iqgualada Formation) below the sampled section have been identified as Middle Eocene in age [Riba, 1976; Puigfàbergas et al., 1992] based on multi-species biostratigraphy. Previous authors also suggest the

Berga Conglomerate Fm. is Eocene to Oligocene in age *i.e.* [Riba, 1976; Ford et al., 1997; Williams et al., 1998; Vergés et al., 2002; Barrier et al., 2010]. The ten magnetozones identified in Figure 11 were correlated with the Geomagnetic Polarity Timescale [Gradstein et al., 2012]. The correlation confirms that the stratigraphic section along route C-462 south of Sant Llorenç de Morunys spans C16n-C12n. Polarity reversal boundaries do not correlate to changes in lithologic or rock magnetic properties and therefore are not.

Knowing absolute ages produced from the magnetic reversal stratigraphy allows for calculation of the average sediment accumulation rates for entire section as well as for each fully constrained reversal chron. Reversal boundaries are constrained to < 15 m and chron boundaries are assumed to be the midpoint between samples. The average sediment accumulation rate for the 1691 m sampled section is 27.8 cm/kyr, and rates for each chron are as follows: C15r: 27.4 cm/kyr (115 m); C15n: 32.8 cm/kyr (100 m); C13r: 18.6 cm/kyr (245 m); C13n: 27.8 cm/kyr (125 m); and C12r: 28.2 cm/kyr (685 m). C16n and C12n are poorly constrained so sediment accumulation rates have not been determined for them.

The principle unconformity occurs within C12r so the calculated sediment accumulation rate for C12r is a maximum rate assuming no non-depositional hiatus. Because beds on either side of the unconformity have reversed polarity we assume that the unconformity remains within the same magnetochron. If the unconformity were instead not record the nearest normal polarity chron C12n and were to end in reversed chron C11r the minimum duration of the unconformity would be the length of C12n, 440 kyr. A large depositional hiatus or erosional removal of material during C12r is unreasonable due to the aggredational nature of the basin. Therefore, the unconformity is likely to remain within C12r and to be relatively short in duration. For all calculations the sediment accumulation rate for C12r

was taken to be the maximum rate of 28.2 cm/kyr.

5.3 Anisotropy of Magnetic Susceptibility (AMS)

Magnetic mineralogy results suggest AMS fabrics are dominanted by paramagnetic clays. AMS fabrics found in the Berga Conglomerate Fm. are similar to those found in deformed fine grained rocks [Borradaile, 1991; Parés et al., 1999; Soto et al., 2009]. Magnetic fabrics recovered from Berga Conglomerate Fm. sand and siltstones record multiple stages of deformation. The first stage is a compactional fabric that is pervasive throughout the region. This fabric has been observed in samples collected > 10 km apart, including nearly flat-lying undeformed exposures. The first fabric is likely formed as a sedimentary compactional where the minimal principal axes are oriented orthogonal to bedding [Parés, 2004; Sintubin, 1994]. This produces an oblate fabric with $\kappa 1$ and $\kappa 2$ randomly oriented along the bedding plane.

A second fabric is a layer parallel shortening (LPS) fabric seen in the orientation of the $\kappa 1$ axis perpendicular to the shortening direction. This fabric is seen in both limbs of the syncline in Figure 8. The $\kappa 1$ orientation is interpreted as an intersection lineation of phyllosilicate grains [Parés et al., 1999; Tauxe, 2010]. As deformation progresses the originally oblate ellipsoid becomes triaxial where $\kappa 3$ remains perpendicular to bedding, $\kappa 1$ rotates to prependicular to the shortening direction, and $\kappa 2$ rotates to parallel to the shortening direction. A later fabric is also seen in the hinge of the main syncline (Figure 8). This fabric rotates the $\kappa 3$ axis to a high angle to the pole to bedding while also producing a girdle in the $\kappa 1$ and $\kappa 2$ axes perpendicular to the N-S shortening direction (Figure 8).

The three competing kinematic models of folding at Sant Llorenç de Morunys

[Suppe et al., 1997; Ford et al., 1997; Alonso et al., 2011] suggest different strain histories. Our AMS data provides an objective method to determine which kinematic model is most likely. Suppe *et al.* [1997] supports a migrating hinge model which would produce differing strain on either limb of the syncline. As the hinge moves through time and space, some sites on the upright limb will record a transition from flat limb to hinge to upright limb. However, the sites on the flat limb in this folding mechanism would have always had the same structural position. Therefore if the folding was controlled by a moving hinge one would expect the two limbs of the fold to record different strain histories. A fixed hinge kinematic model [Ford et al., 1997] predicts a different strain history. Limbs in a fixed hinge fold always retain the same structural position through time. Thus, both limbs would experience similar deformational histories, only the magnitude of their rotation would be different. AMS data shows no evidence of a significant difference in the flat lying and upright limbs except for the degree of bedding rotation (Figure 8). The similar strain histories of both limbs is interpreted as evidence for fixed hinge kinematics as suggested by Ford *et al.* [1997].

5.4 Rock Magnetic Cyclostratigraphy

A robust cyclostratigraphy, with significant spectral peaks at expected Milankovitch periods, based on χ variations has been developed for the Berga Conglomerate Fm. (Figure 13). This cyclostratigraphy spans from 31.6 Ma within the largest conglomerate in the El Castell Formation to 34.4 Ma at the contact between the El Bastets and Sobirana Formations at total stratigraphic distance of 653.4 m. Low temperature χ measurements indicate that paramagnetic minerals dominate the mixed magnetic mineralogy in controlling χ variations. Because of the terrestrial nature of the Berga Conglomerate Fm. the paramagnetic minerals are interpreted

to be clays formed by the weathering of source material. The Berga Conglomerate Fm. shows evidence of extensive weathering typical of terrestrial redbeds that would suggest paramagnetic clays as a likely source of χ variations.

Magnetic reversal stratigraphy provided coarse sediment accumulation rates for correlation of spectral peaks to absolute time. Tuning the χ data series to modeled orbital obliquity for the Eocene - Oligocene allows corrections for variable sediment accumulation rates. Obliquity tuning was selected because of a strong spectral significance and high resolution. This cyclostratigraphy provides 20 kyr resolution for structural reconstruction of deformation caused by the fault propagated fold. Tuning to theoretical obliquity [Laskar et al., 2004] reduces noise caused by sediment accumulation variations (Figure 12). It also enhances percessional scale index by eliminating some peaks and enhances signal at 25.7 and 20 kyr frequencies. Additional tunes at short eccentricity (97-120 kyr) and long wavelength (>90 kyr) time scales were attempted for the data series. However, these did not significantly improve Milankovitch scale frequencies.

5.5 Climate Encoding

Encoding mechanisms are difficult to determine in χ based cyclostratigraphy because of the interactions of many magnetic minerals. χ based cyclostratigraphy suggests that these climate variations are being encoded and results from magnetic mineralogy and AMS analyses suggest that variations in paramagnetic clays dominate the χ signal. However, bulk χ analyses do not provide a method to unravel climate encoding. Therefore, the G / (G + H) ratio is used in this study to recover the climate signal of the region during or shortly after sediment deposition. G / (G + H) variability has been shown to be related to wet and dry climate vairations

[Yapp, 2001; Harris and Mix, 2002; Abrajevitch et al., 2009]. Detailed soil studies [*e.g.* Kämp and Schwertmann, 1983; Sangode and Bloemendal, 2004] suggest that the G / (G + H) ratio is independent of parent material and therefore is only influenced by climatic factors. As shown in Appendix Figure 2 the G / (G + H) ratio recovers multilevel frequency variations related to long scale climate changes in depositional environment. This suggests that variations in χ are likely due to variations in phyllosilicate concentration driven by climatic cycles.

5.6 High-resolution Tectonics and Sedimentation Rates

Kinematic controls on the fold growth and therefore fault growth can be infered by understanding how growth strata were formed [Suppe et al., 1992]. The 20 kyr resolution obtained from our tuned cyclostratigraphy was applied to both sediment accumulation and fold growth to examine the interaction of both on growth strata formation. Sediment accumulation rates at 20 kyr and magnetic reversal chron scales are shown in Figure 14. Cyclostratigraphy based accumulation rates vary from 0.10 - 0.37 m/kyr and average 0.24 m/kyr. Both the chron averaged and 20 kyr resolution methods predict similar accumulation rates in sites younger than 33,250 kyr. However, the two methods predict slightly different rates in older rocks as the chron averaged rate overestimates the sediment accumulation rate. Folding history at both 20 kyr and magnetic reversal chron scales are shown in Figure 15. Cyclostratigraphy based folding rates vary from 0 - 2 °/20 kyr. Chron averaged rates over estimate the % folding for most of the section and are also artificially steady. 20 kyr resolution determined from magnetic cyclostratigraphy recovers a much more unsteady deformational history. The 20 kyr record displays two periods of low tectonic activity from 33,400-34,400 kyr and from 32,600-33,100 punctuated by periods of rapid folding. Sediment accumulation and folding rates

correlate 29 % of the time, *i.e.* both accumulation and folding are in sync 29 % of the time.

These results illustrate the difference between magnetochron averaged and high resolution cyclostratigraphy rates for understanding deposition and deformation. Higher temporal resolution recovers more variability in both sediment accumulation and percent of total folding of the Berga Conglomerate Fm. This suggests that long timescale depositional or deformational histories do not recover the complete variance of intrinsic behavior. In order to capture variations at 10^4-10^5 yr a sufficiently fine time resolution is needed. In both sediment accumulation and percent of total folding cyclostratigraphic histories recover a higher frequency and variability in change. Sediment accumulation cyclostratigraphic histories show high frequency variance in accumulation rate not captured in chron averaged time scales. Folding cyclostratigraphic histories display tectonic quiescence which is not recovered in longer time scale reconstructions. The resolution of our depostional and deformational histories is limited to 20 kyr.

5.7 Structural Modeling

The Fault-Fold v 6 software package from Richard Allmendinger [Allmendinger, 1998; Hardy and Allmendinger, 2011] was used to convert fold growth to fault propagation. This software package allows for forward and inverse modeling of fold growth related to trishear faulting [Erslev, 1991]. We will follow the approach of Hardy and Ford [1997] as our modeling constraints. Parameters related to timing of sedimentation and folding has been obtained from the high resolution cyclostratigraphy and is supplemented by AMS kinematic controls.

Faults were modeled with trishear geometries as follows: faults are thrusts that

step up from horizontal detachments, the ramp angle is 15°, the trishear angle is 5°, the propagation to slip ratio is 1.61, and models are run at 20 kyr steps (Figure 16). Results of one model run is shown in Figure 17. This model has geometries that broadly agree with earlier models generated by Ford *et al.* [1997]. Trishear folding predicts stratal geometries which record subtle changes in bedding orientation. This agrees with field observations related to minor unconformities present in the section. Modeled slip rates vary from 115 - 265 m/Myr. Modeling reveals that pauses in sedimentation during folding lead to angular unconformities. This is indicative of times when rapid folding outpaces sediment accumulation. Because sediment accumulation is fairly constant throughout the section fault slip rates have a major control on the location of these minor unconformities.

6 Conclusions

A high-resolution time scale based on Milanikovitch orbital frequencies was recovered from χ in terrestrial foreland facies. χ based cyclostratigraphy is an objective and robust method of timing in terrestrial systems that have sufficient sediment accumulation and accommodation space such as foreland basins. This cyclostratigraphy of the Berga Conglomerate Fm. allows for timing of deformation and sediment accumulation at 20 kyr resolution. Encoding of χ based cyclostratigraphy is less straight forward than ARM studies, but additional characterization using rock magnetics or geochemistry can provide encoding details.

New magnetostratigraphy confirm an Eocene - Olgiocene age to the Sant Llorencç structure and Berga Conglomerate Fm. in agreement with prior interpretations. Rock magnetic analyses identify three ferromagnetic minerals which contribute to magnetostratigraphy remanence, magnetite, hematite, and goethite. χ variations

also include paramagnetic clay contributions, which dominate the χ signal. Correlating the χ data series to magnetostratigraphic time and tuning to theoretical obliquity [Laskar et al., 2004] removes the effect of variable sediment accumulation and improves signals at precessional and long eccentricity time scales. The timing constructed from this age model was then used for structural interpretations. AMS data support a fixed hinge and flexural slip folding kinematics associated with blind thrust faulting.

I have recovered the onset of deformation of the Sant Llorenç structure at 33.854 Ma and provided a maximum depositional hiatus of 400 kyr for the principal unconformity. The age model predicts little correlation between sediment accumulation and fold deformation. As shown in Figure 14 sediment accumulation rates are fairly constant throughout the entire rock magnetic section. Folding rates are much more variable (Figure 15) and appear to be separated into long periods of quiescence punctuated by rapid changes. This suggests that deformation in this region is not driven by changes in sediment supply, but rather by changes in tectonic activity. Model derived fault slip rates vary from 115 - 265 m/Myr. Both structural modeling and cyclostratigraphic timing support highly variable fold deformation through geologic time. High-resolution timing reveals more variable folding rates than recovered at magnetochron time scales. This speaks to the unsteadiness of fault related folding and how sufficient resolution is needed to recover high frequency variability in fault slip. Rock magnetic cyclostratigraphy therefore is a useful tool in providing the timing resolution needed to examine these rapid changes in fold geometry.

7 Figures

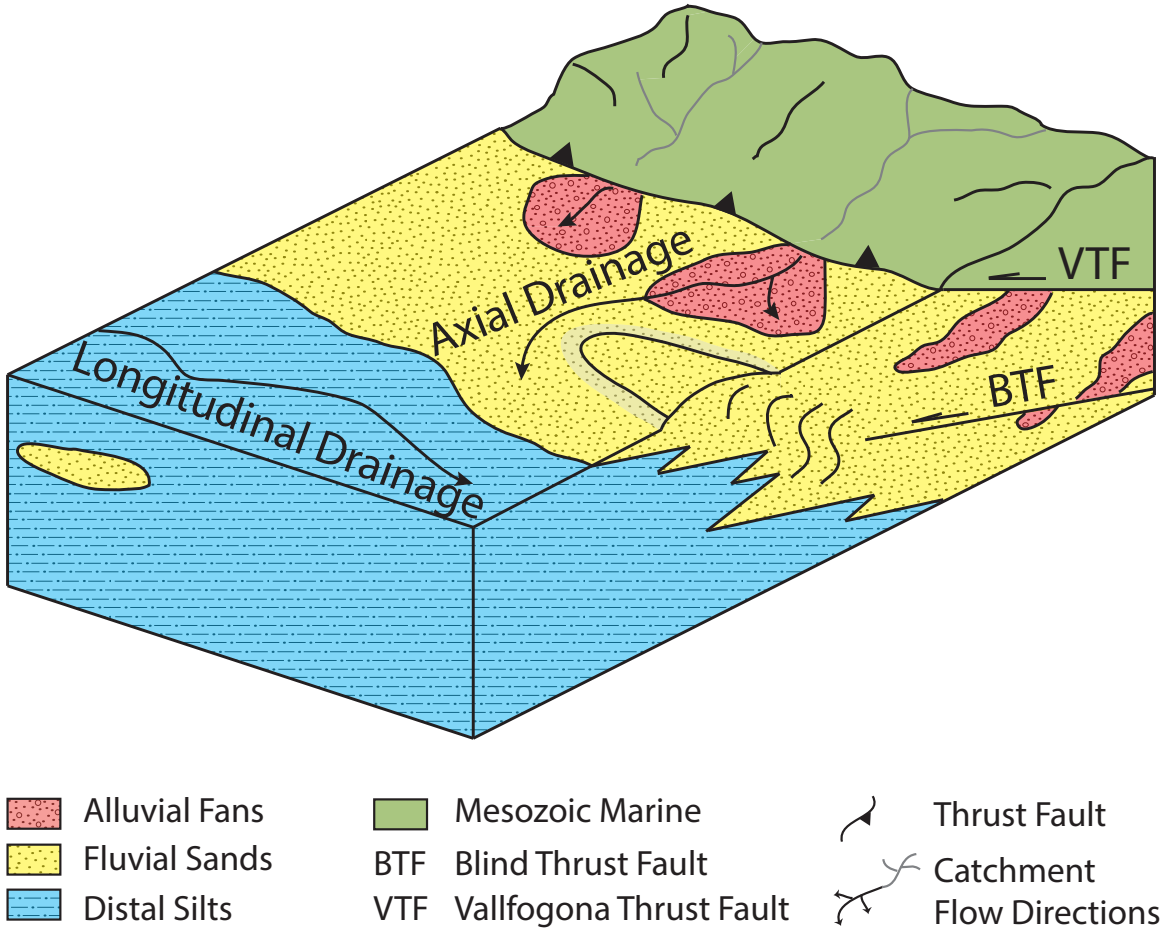

Figure 1: Schematic block diagram showing the depositional environment during the formation of the Sant Llorenç structure. The depositional environment is controlled by long term climate variations as well as the changing position of axial and longitudinal drainage of the region. Modified from Barrier *et al.* [2010].

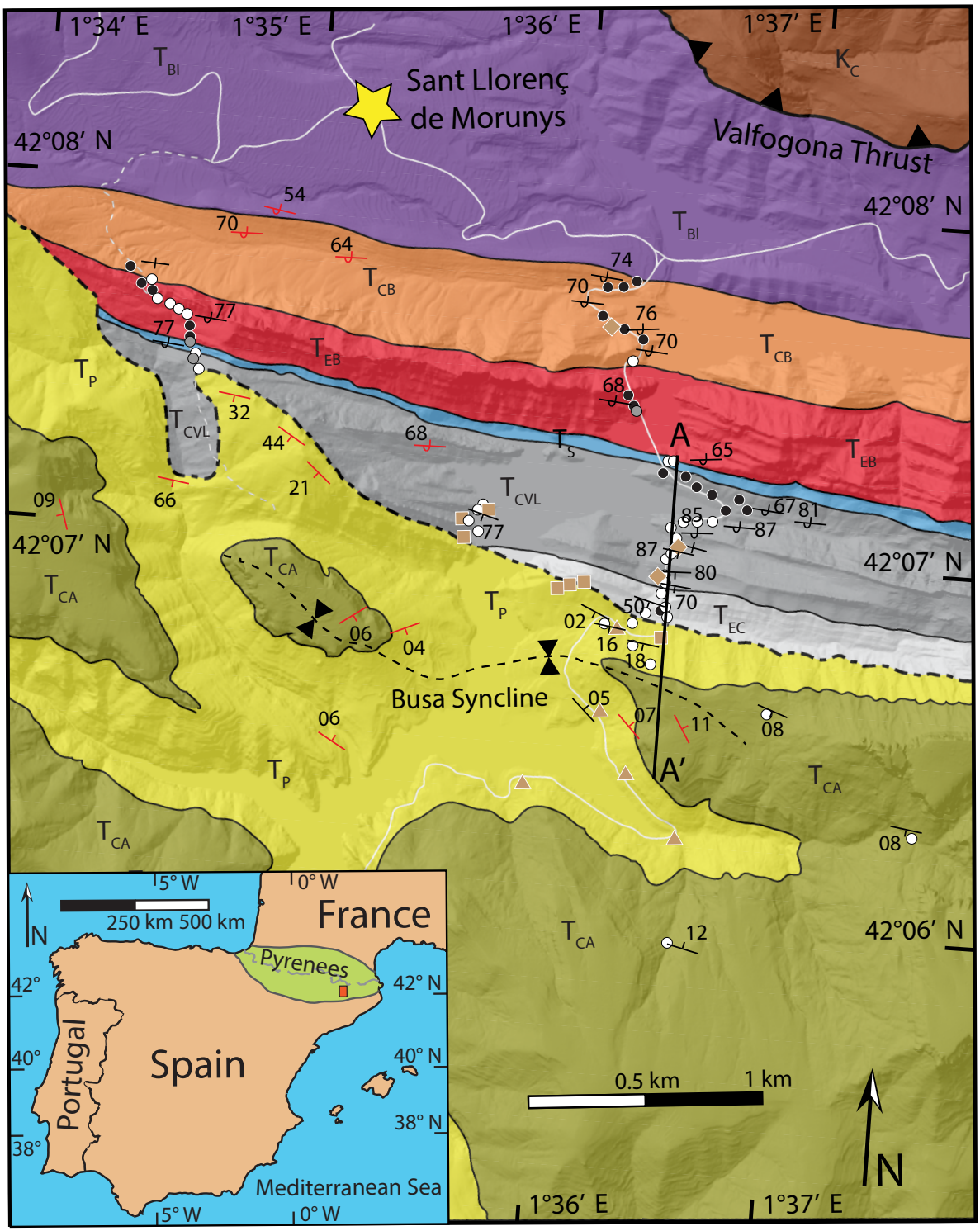

Figure 2: Geologic map of Sant Llorenç structure and surrounding area. Map units are described in Section 2 and the line of cross section shown in 8 is indicated. A full legend is found on the following page.

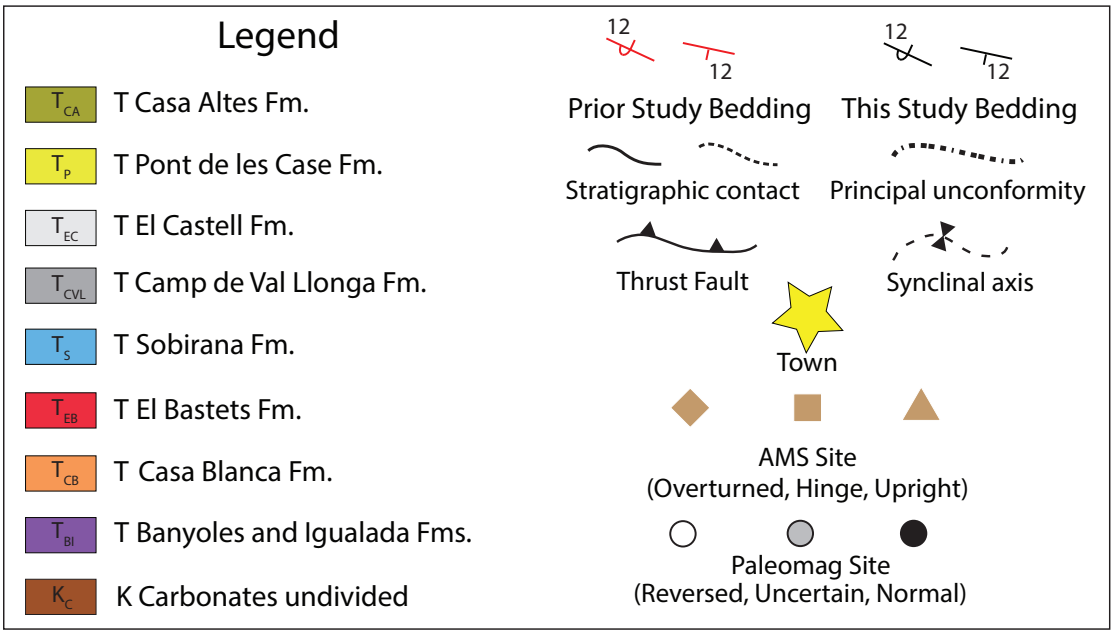

Legend for Figure 2.

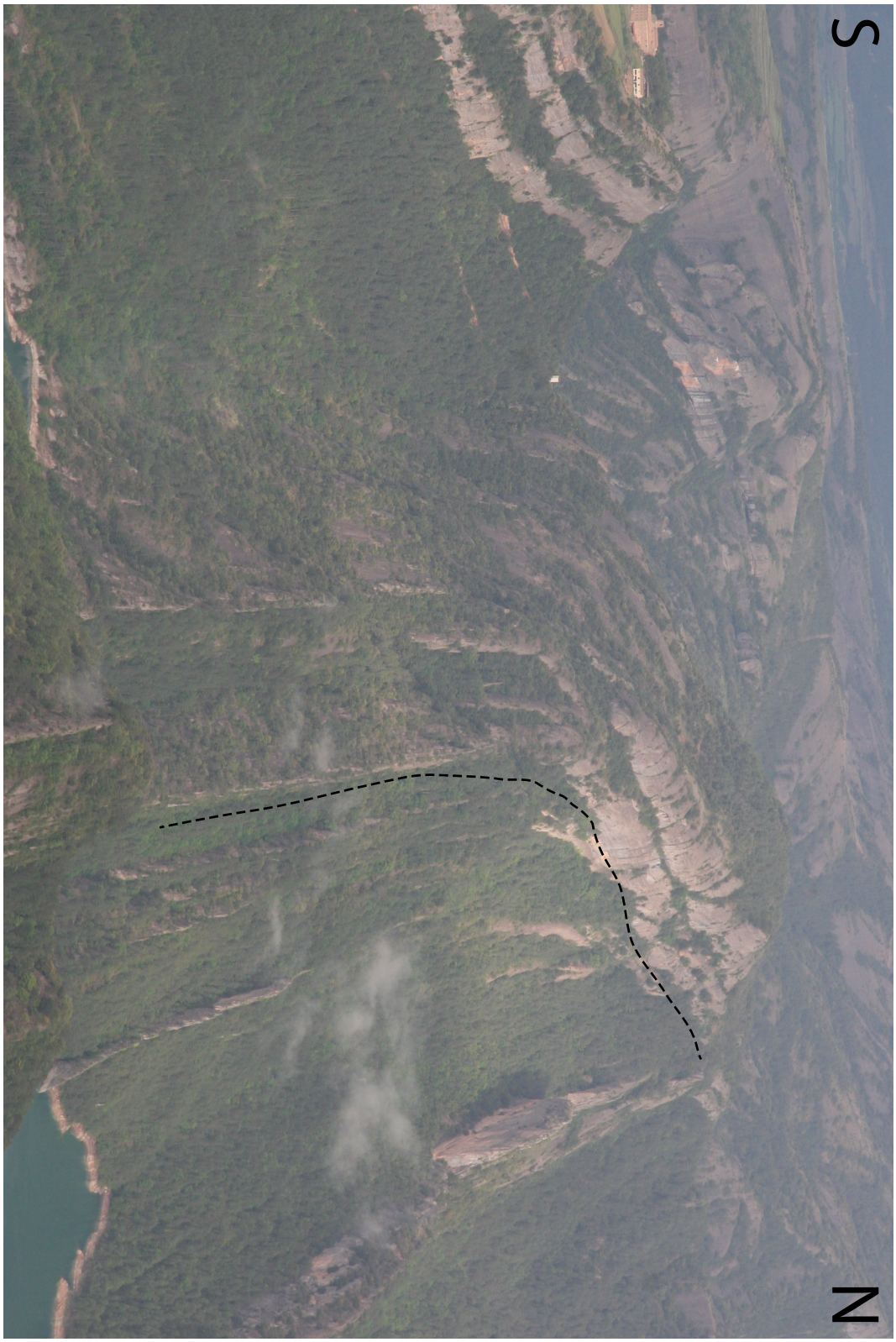

Figure 3: View west along bedding strike of fault related folding at Sant Llorenç de Morunys. The location of the principal unconformity is shown as the dashed line. Note the change in stratigraphic position of the unconformity and its progression from angular unconformity to disconformity upsection. This location is the archetypal angular disconformity of Suppe *et al.* [1997]

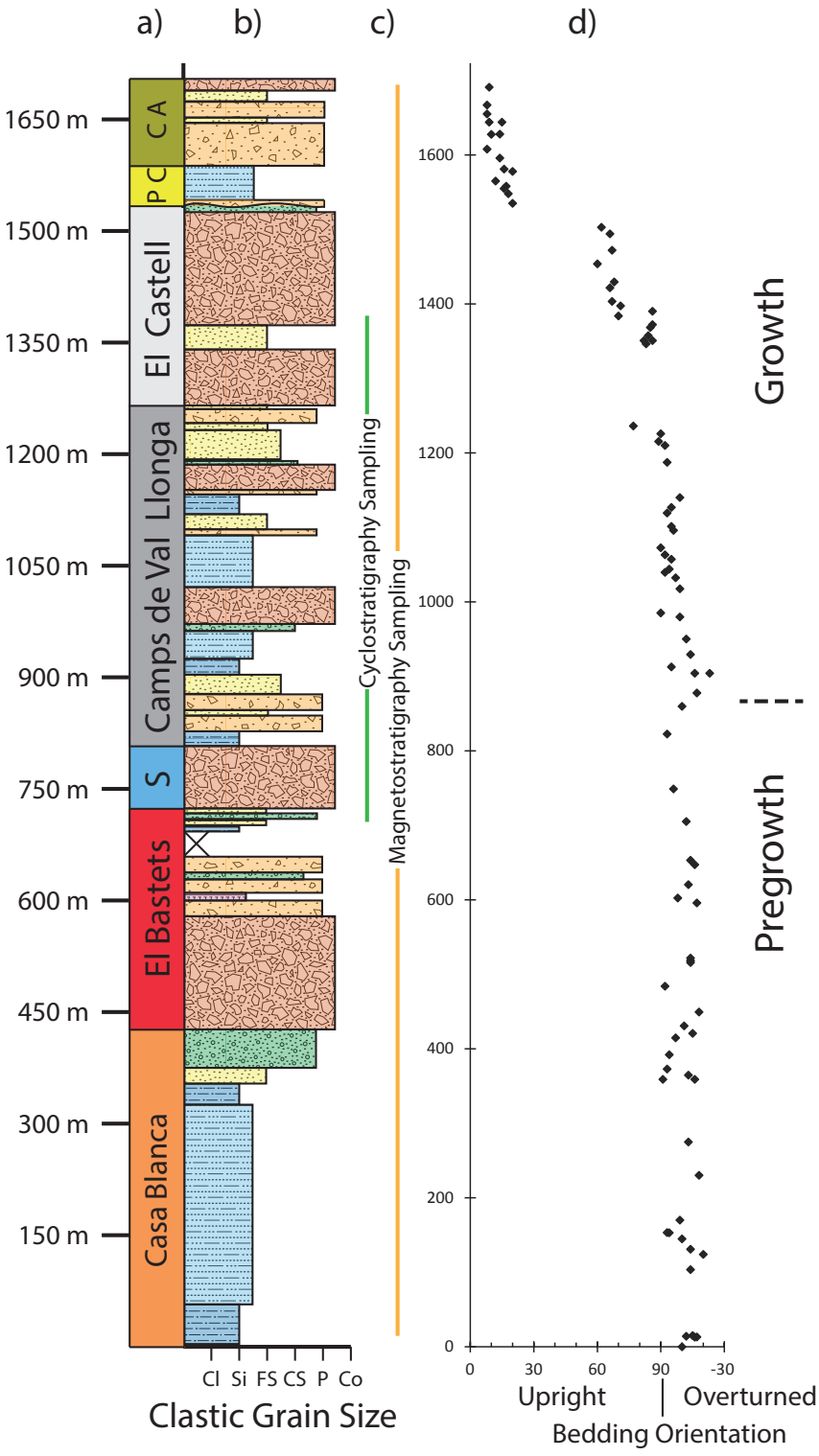

Figure 4: Stratigraphic column for the Berga Conglomerate Formation sampled in this study. a) Unit formations b) lithologic variations follow the facies designations of Barrier *et al.* [Barrier et al., 2010]. c) Extent of χ cyclostratigraphic and magnetostratigraphic sampling (Figure 10). d) Bedding inclination with growth and pregrowth sections indicated. See Appendix Figure 9.3 for a more detailed lithostratigraphic column.

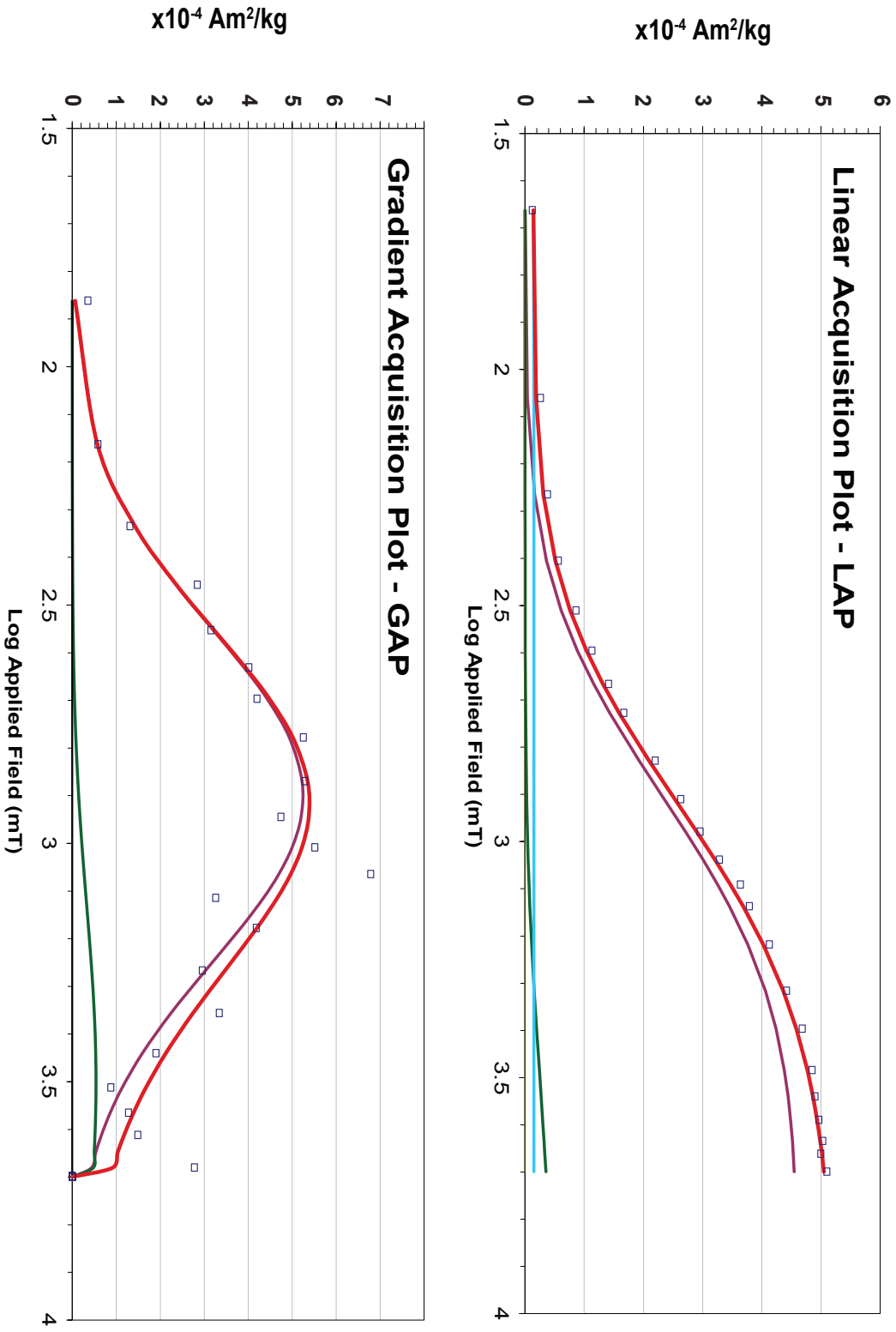

Figure 5: IRM acquisition modeling [Kruiver et al., 2001] for sample BUSA-147, a fine grained sandstone. Linear acquistion plot (LAP) and the gradient acquisition plot (GAP), which is the first derivative of the LAP, are shown. Both plots show a three component field dominated by one component (pink).

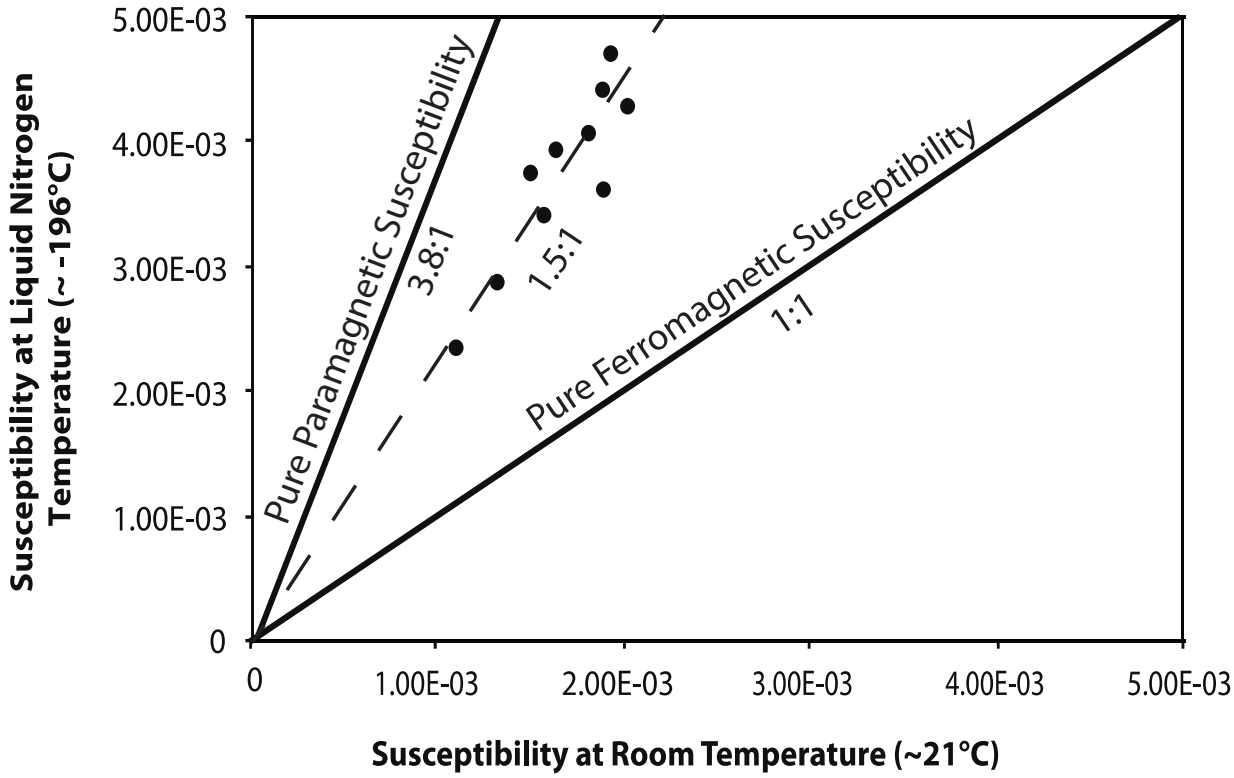

Figure 6: A comparison of susceptibility at room and liquid nitrogen temperatures. Specimens plot between the paramagnetic and ferromagnetic fields indicating a mixed magnetic mineralogy, which agrees with Figure 5. The ratios expected enrichment ratio for pure paramangetic and ferromagnetic minerals are shown for reference.

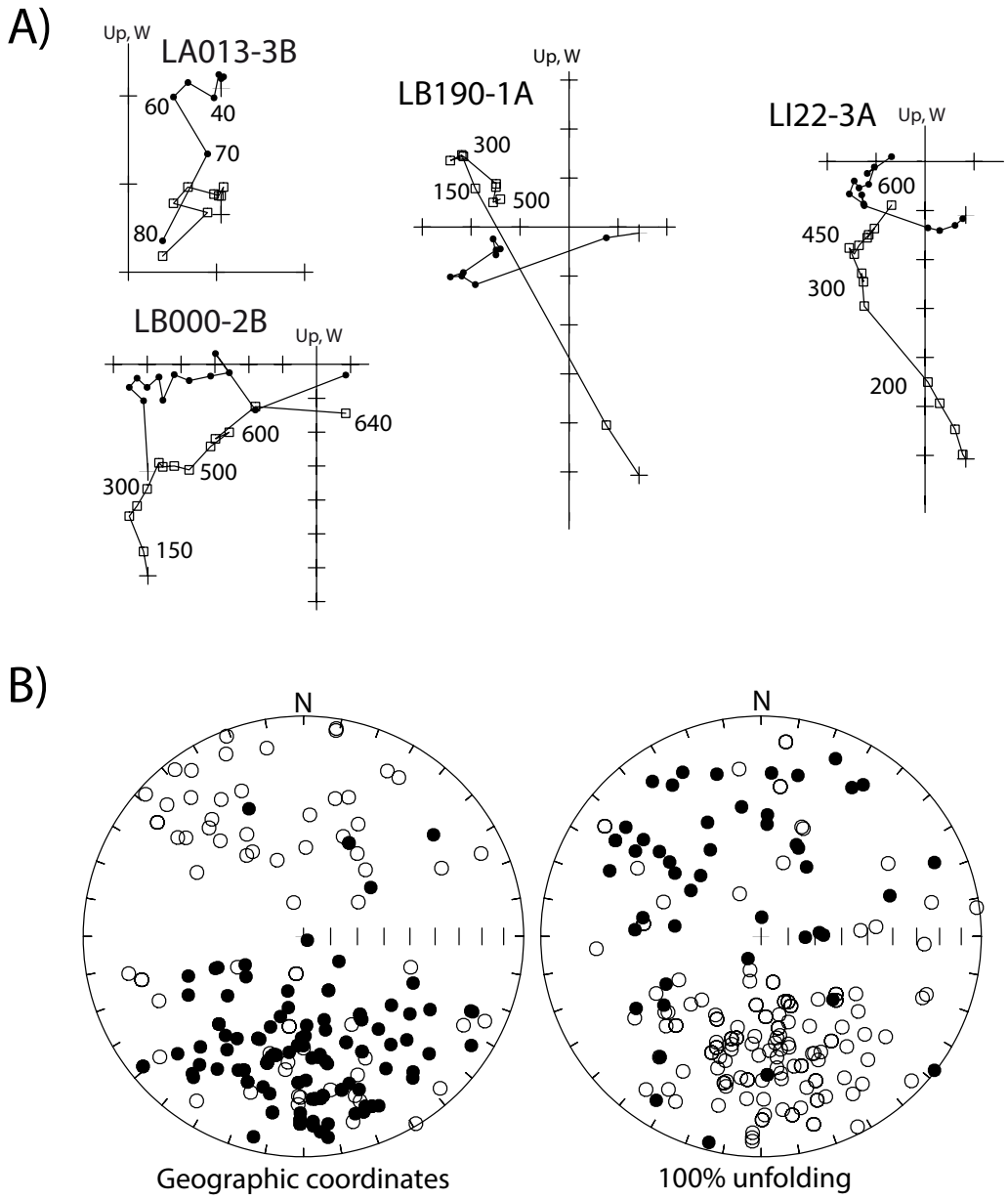

Figure 7: (A) Vector end point diagrams for four paleomagnetic samples plotted in geographic coordinates, following Zijderveld [1967]. The data points represent a particular demagnetization step projected onto the horizontal (solid dots) and the vertical planes (open squares). Numbers indicate temperature at that point in degrees Celsius except for specimen LA013-3B where they indicate the alternating field strength in mT. Thermal demagnetization provided better results than alternating field demagnetization and was used for a majority of specimens. (B) Equal area projection of Characteristic Remenance Magnetization (ChRM) directions in geographic coordinates and after 100 % unfolding. Sites projected unto the lower hemisphere are indicated by filled circles and sites projected unto the upper hemisphere are indicated by open circles.

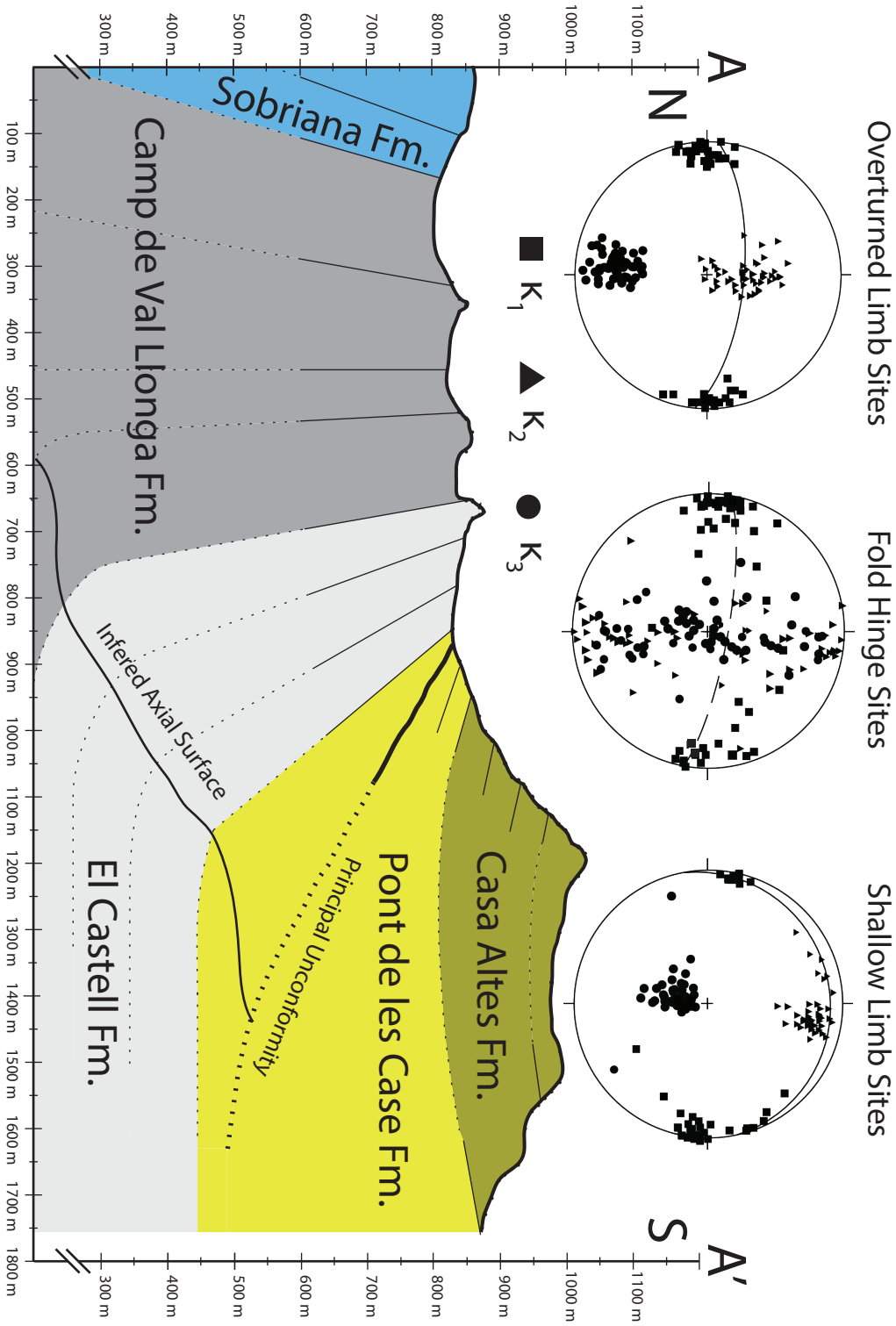

Figure 8: Cross section showing AMS data grouped into steep limb (SLM 4, 5, 8, 9, 10, 17, LA, LC, and LD), hinge (SLM 3, 6, 11, 12, 13, 18, 19, 20, and 21), and upright limb (SLM 1, 2, 7, 14, 15, and 16) to show variations in fabric across the main syncline. Principal axis $\kappa 1$ (squares), $\kappa 2$ (triangles), $\kappa 3$ (circles), bedding plane (solid line) and cleavage plane (dashed line) are plotted in geographic coordinates on equal area, southern hemisphere projections for each region.

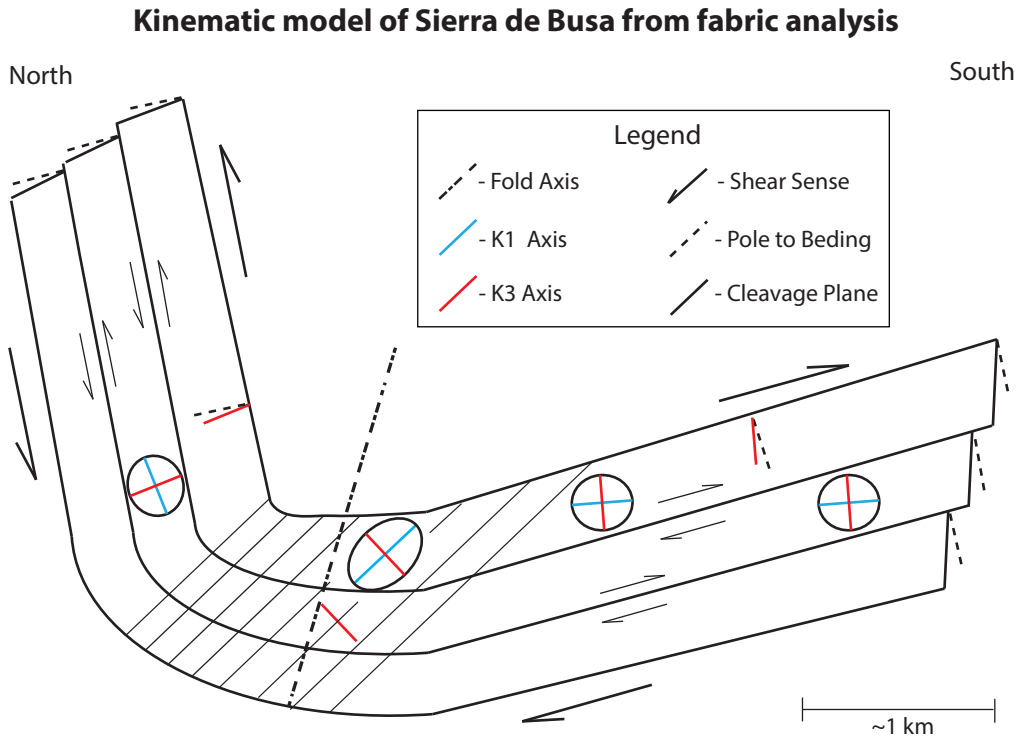

Figure 9: A model of AMS and mesoscopic fabrics observed in the Sierra de Busa syncline. In the hinge of the syncline the $\kappa 1$ axis denotes a cleavage plane. AMS fabrics suggest both flexural slip and flexural flow deformation mechanisms contribute to development of the syncline.

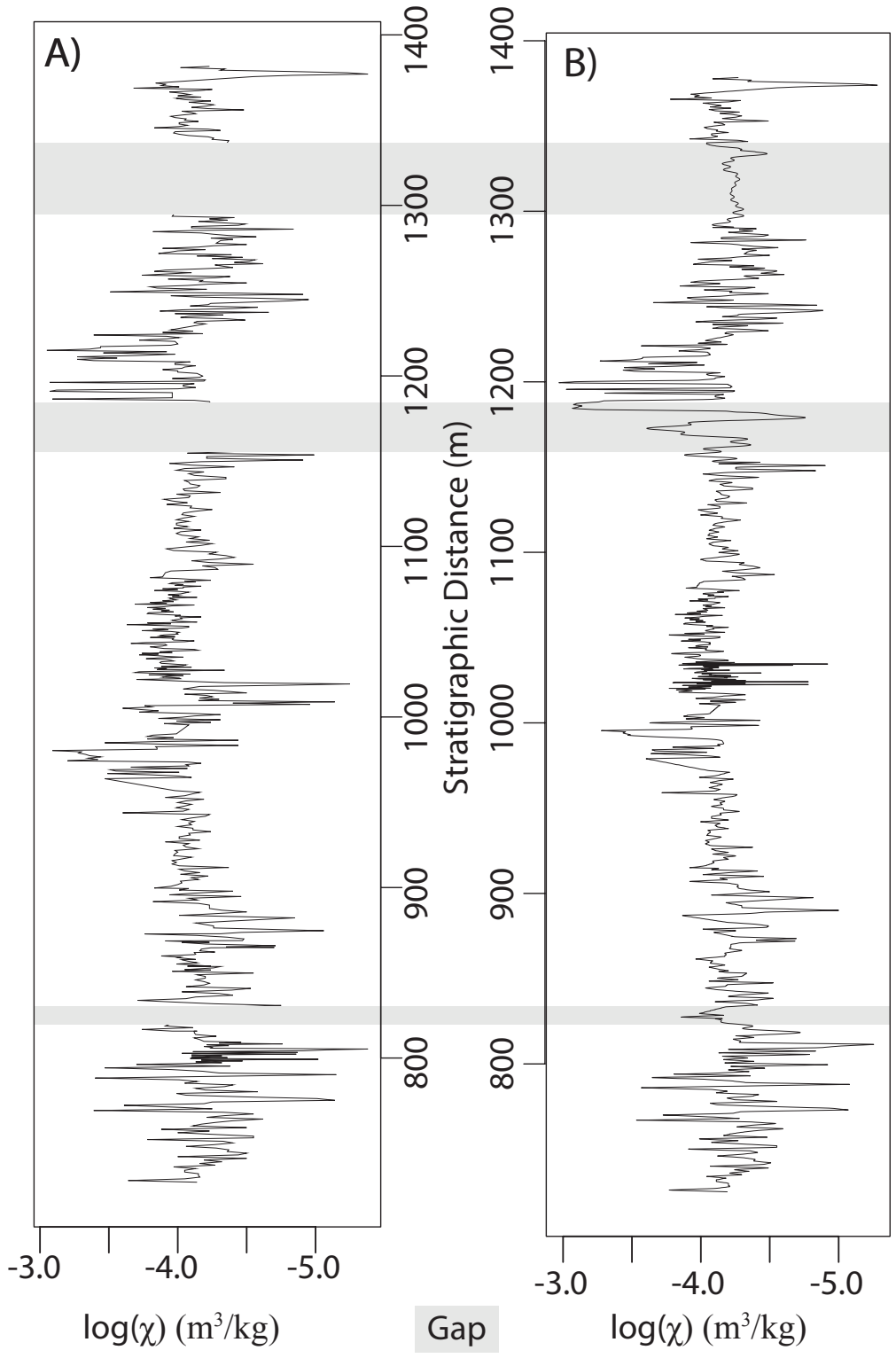

Figure 10: Volume normalized χ data series for extent of rock magnetic sampling as a function of stratigraphic distance. A) Shows the original data where gaps are indicated by the grey regions. B) Shows the same data with gaps filled by SSA fitting [Ghil et al., 2002].

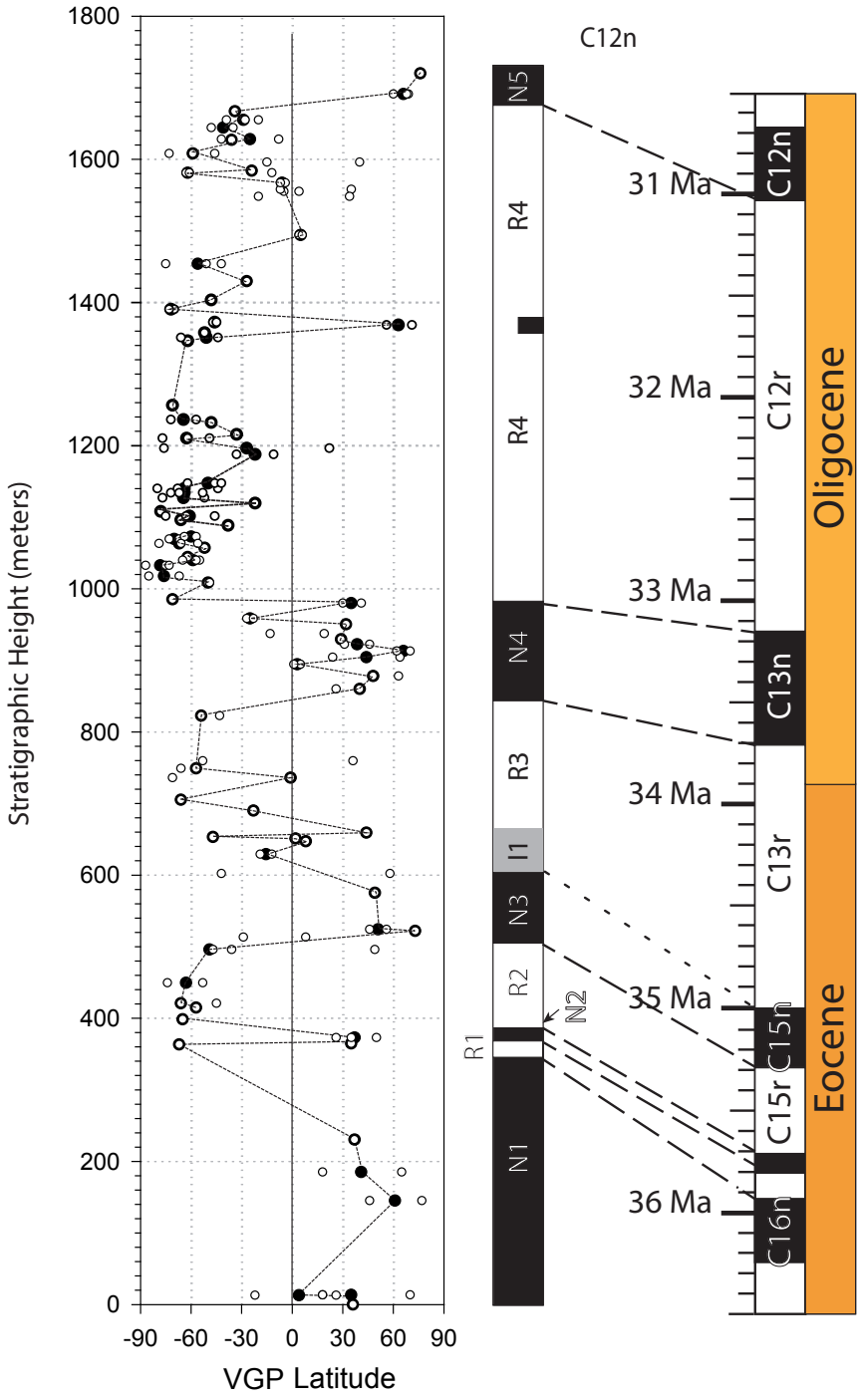

Figure 11: Virtual geomagnetic pole (VGP) latitudes and correlation to the geomagnetic polarity timescale GPTS2012 [Gradstein et al., 2012]. Sites that have an opposite polarity from surrounding sites are indicated with a half bar of the corresponding polarity. Solid circles are site means and open circles are individual specimens. Dashed lines show correlations with strong confidence and dotted lines show plausible correlations.

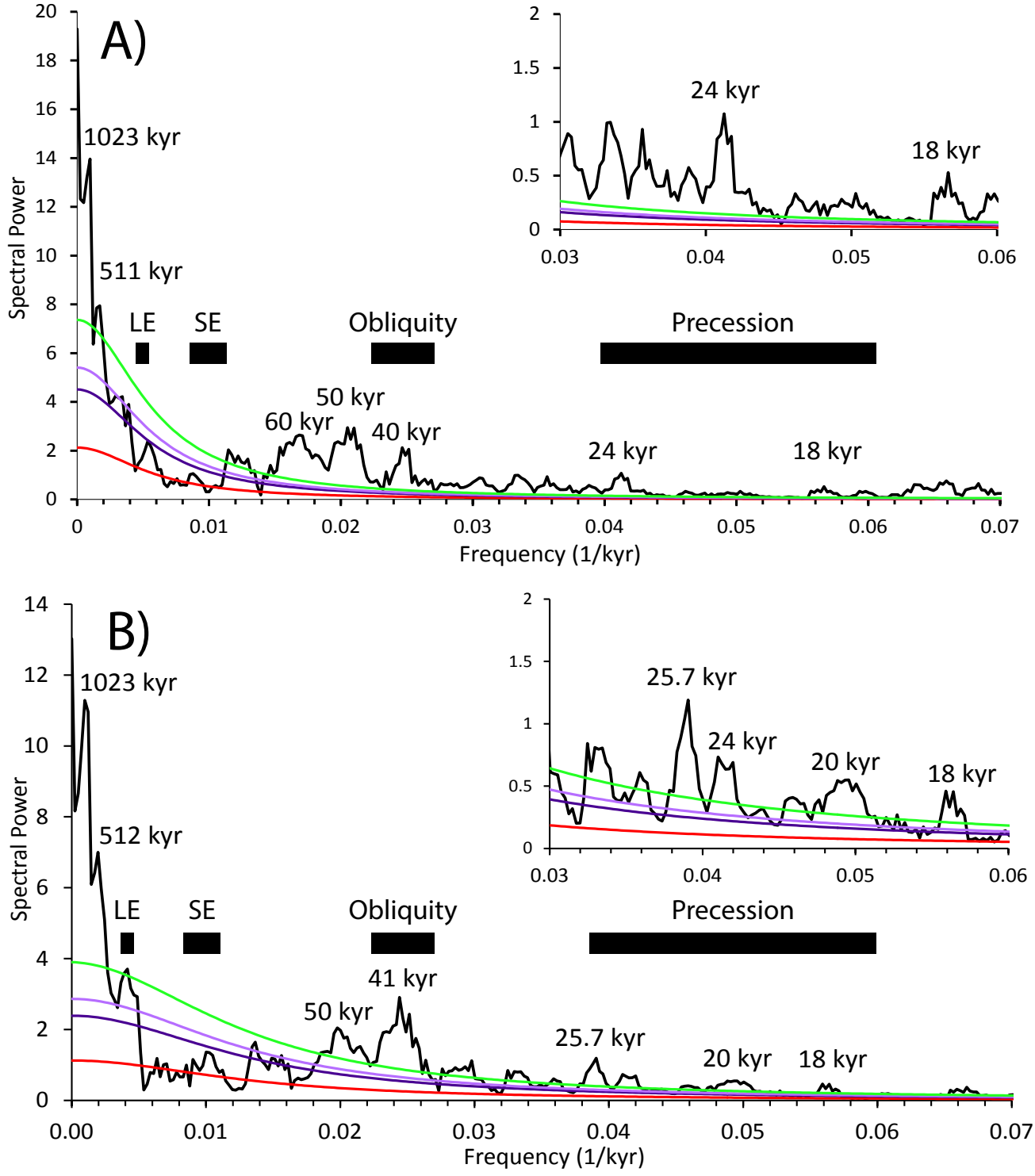

Figure 12: (a) MTM spectral analysis of the un-tuned χ data series. The red curve indicates the robust red noise [Mann and Lees, 1996], and the violet, light purple, and green curves, indicate the 90%, 95%, and 99% confidence intervals respectively. Significant spectral peaks are identified. (b) MTM spectral analysis of the tuned χ data series. Peaks without expected Milankovitch periodicities lose significance after tuning to theoretical obliquity. Both (a) and (b) have an inset from 0.03 - 0.06 to better display expected precessional frequencies.

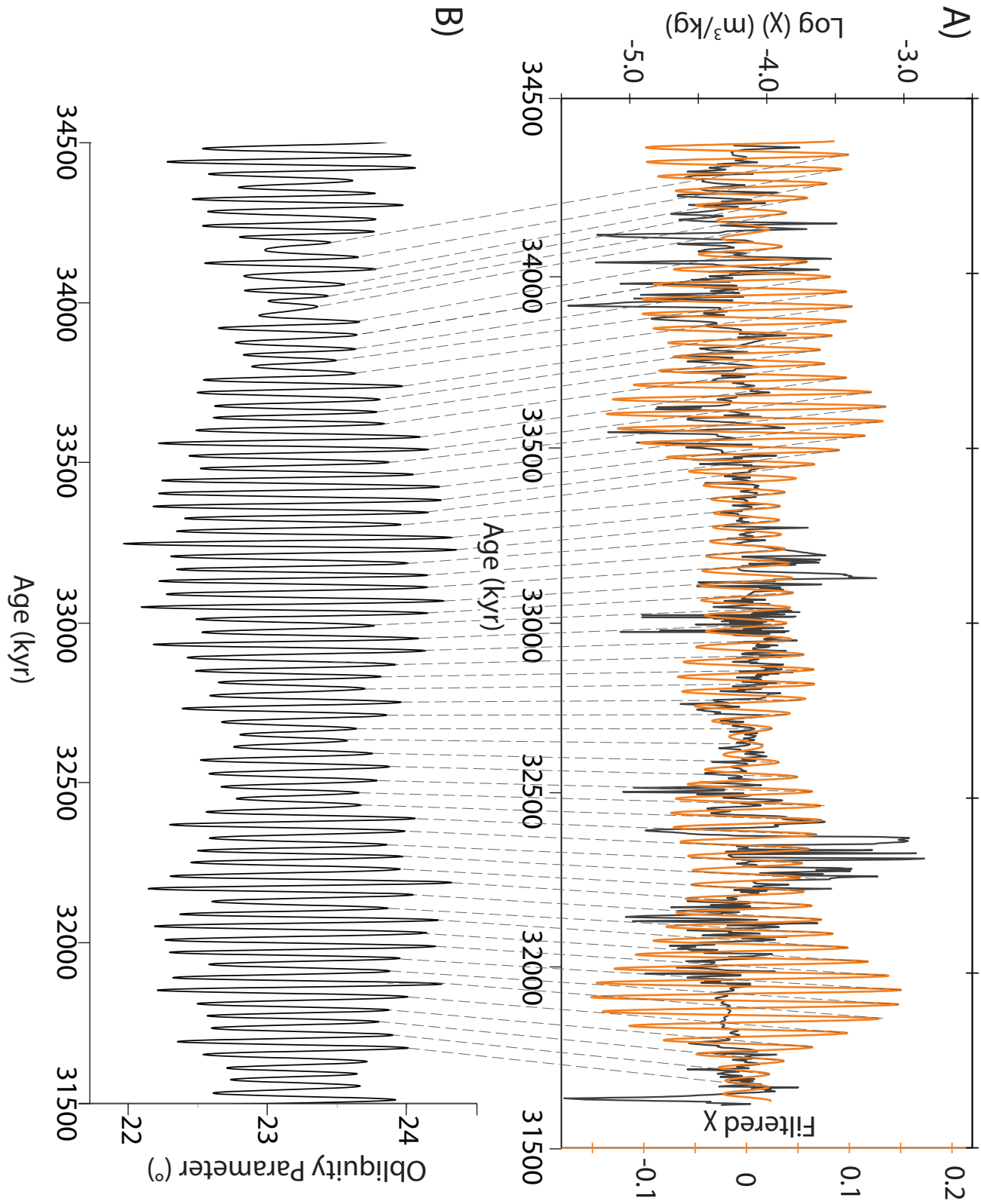

Figure 13: Correlation of χ data series to theoretical obliquity model of Laskar *et* al. [2004]. A) The χ data series (black) was filtered at obliquity, 41 kyr, (orange) to allow for correlation to the theoretical model. Correlations between filtered data and theoretical obliquity (B) are dashed for clarity.

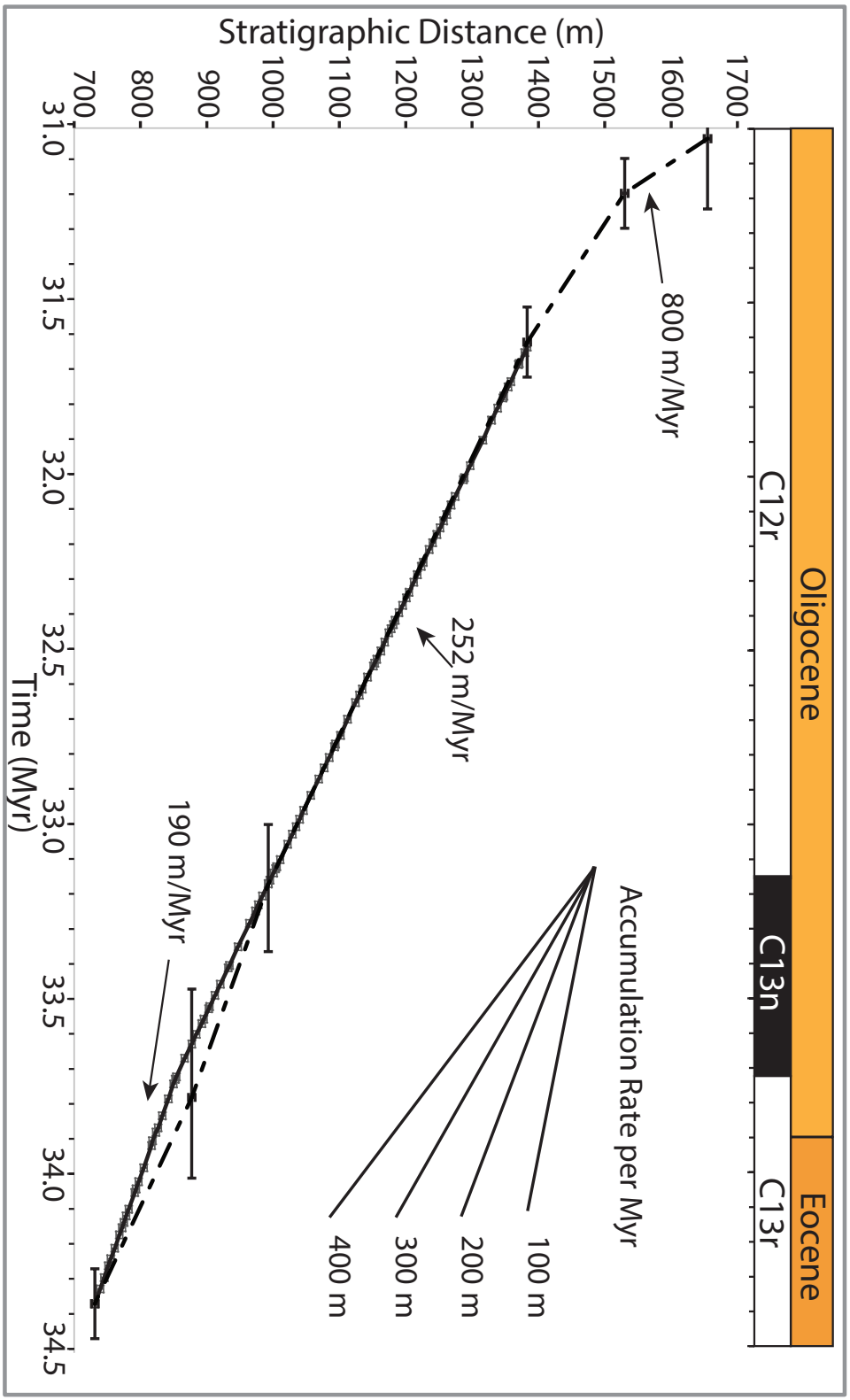

Figure 14: Sediment accumulation correlated to precessional (solid) and magnetochron (dashed) time scales. Accumulation rates are determined by using the slope of the curve inserted scale. Error bars show absolute timing uncertainties and stratigraphic location precision.

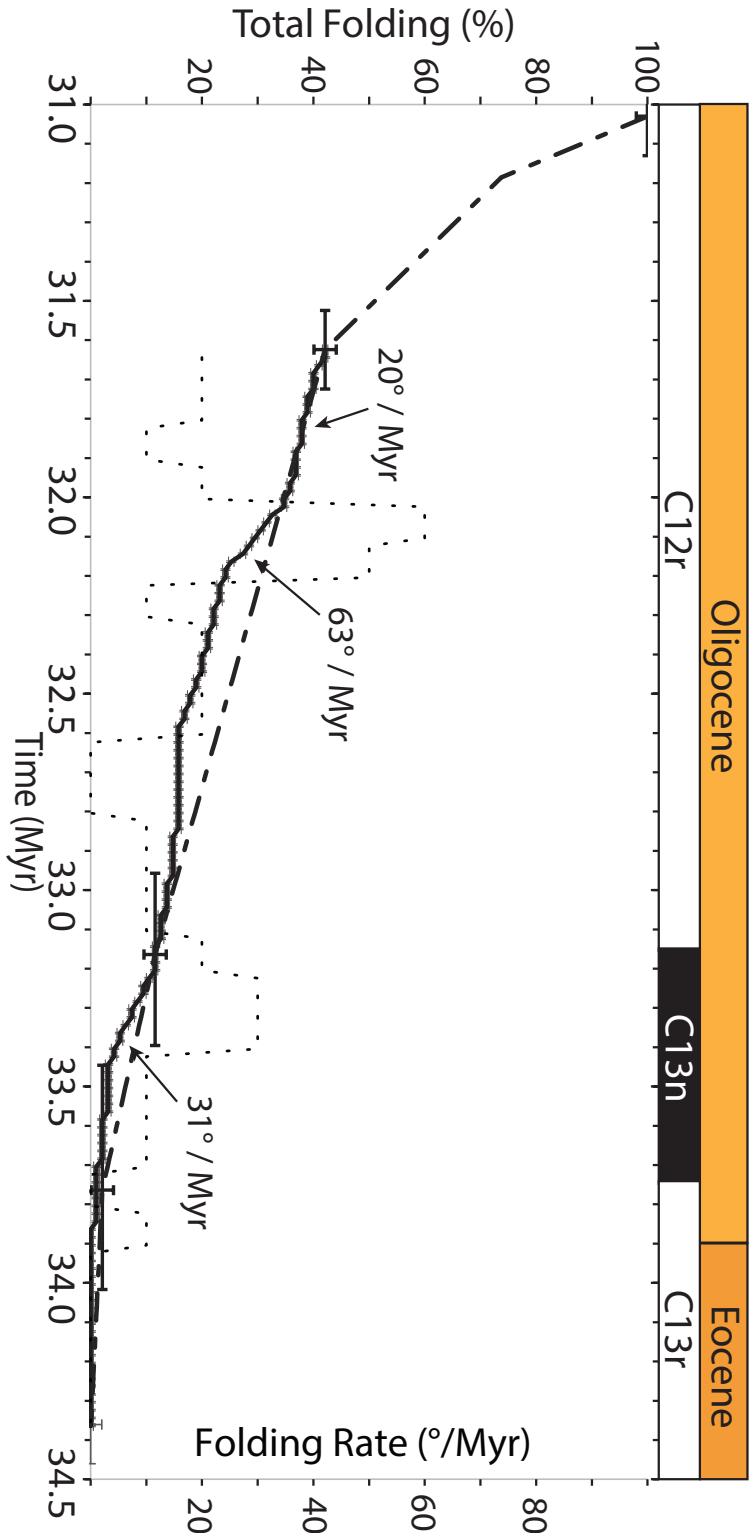

Figure 15: Percent folding as a function of time at precessional (solid) and magnetochron (dashed) scales. Error bars for both methods are displayed. Limb tilt rates can be calculated by using the provided lines and selected rates are displayed.

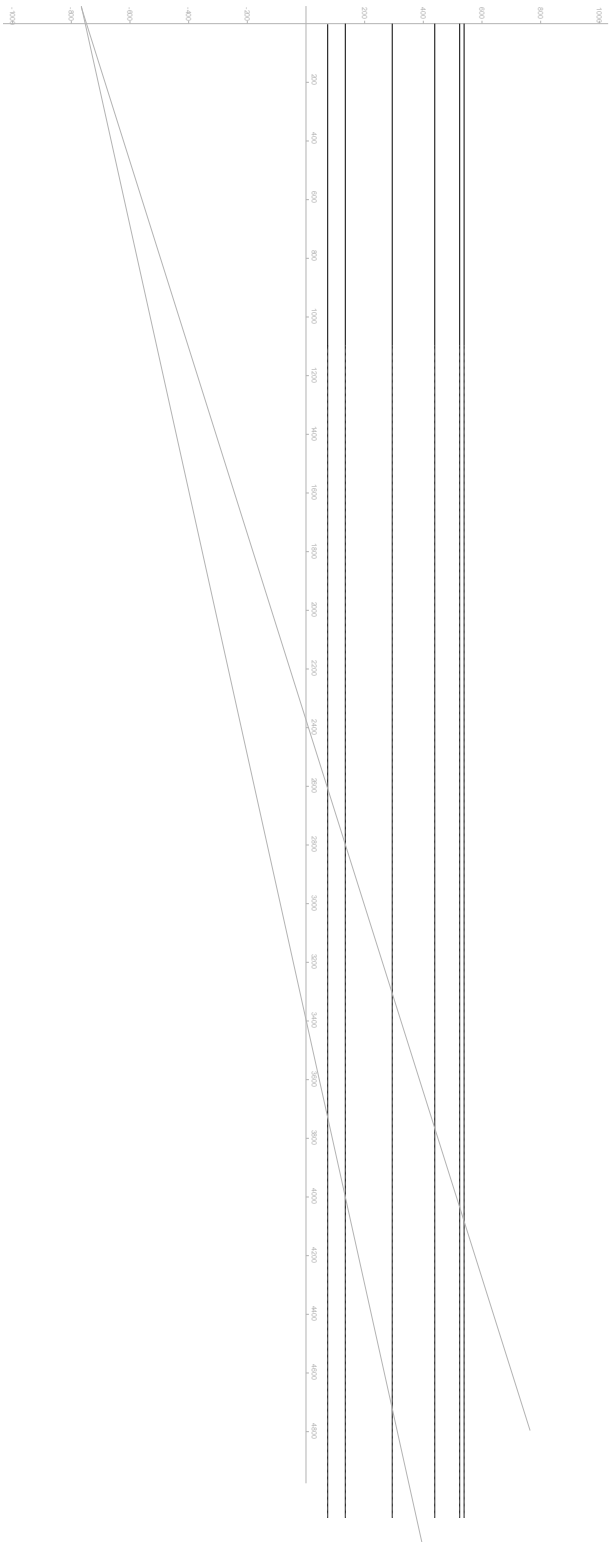

Figure 16: Intial condition of the Fault-Fold modeling run. the ramp angle is 15°, the trishear angle is 5°, the propagation to slip ratio is 1.61, and models are run at 20 kyr steps. Intial beds at 375, 425, 575, 725, 800, and 825 m were selected based on major lithologic changes.

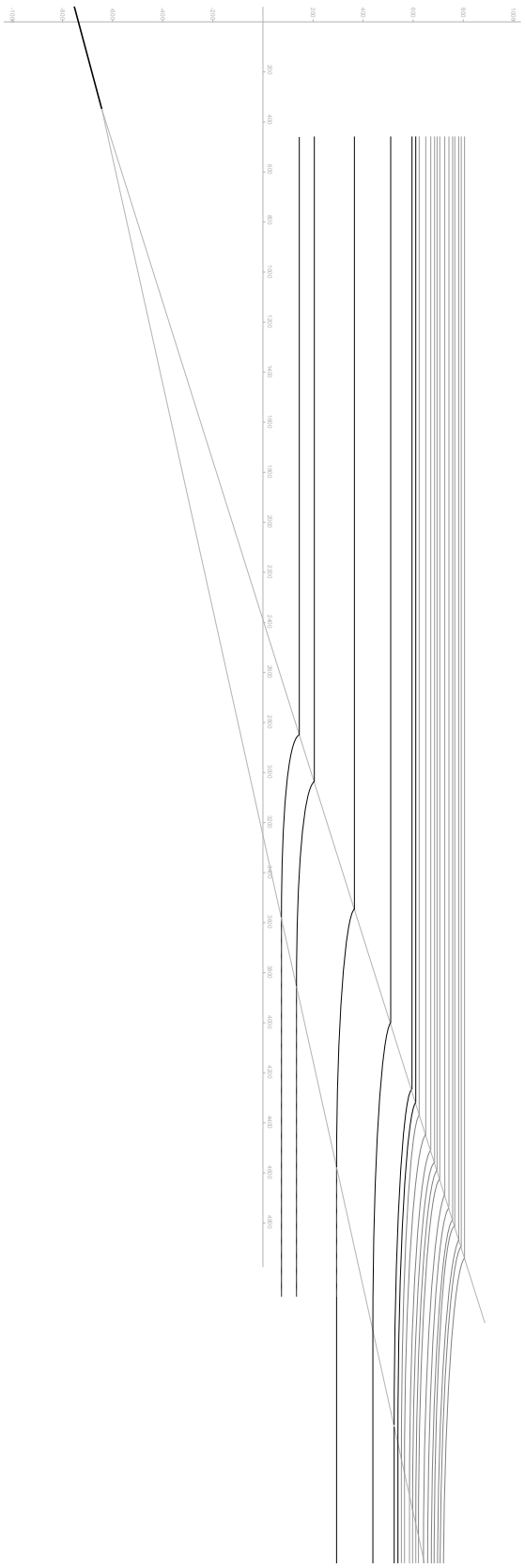

Figure 17: Results of an individual Fault-Fold modeling run. Model ran for extent of cyclostratigraphic time constraint, 2.734 Myr. Sediment was added based on predicted sediment accumulation rate from Figure 14.

8 Tables

Structural Position	Site	κ 30 ℃	κ -197 ℃	κMax	κInt	κMin	P´	T
Upright Limb	SLM 1	1.25E-03	2.50E-03	1.0117	1.0037	0.9846	1.0286	0.4456
Upright Limb	SLM 2	1.12E-03	3.73E-03	1.0115	1.0038	0.9847	1.0293	0.3080
Upright Limb	SLM 7	1.55E-03	4.72E-03	1.0109	1.0007	0.9884	1.0229	0.0630
Upright Limb	SLM 14	1.22E-03	N/A	1.0226	1.0049	0.9725	1.0527	0.3059
Upright Limb	SLM 15	1.71E-03	N/A	1.0295	1.0062	0.9664	1.0660	0.2009
Upright Limb	SLM 16	1.64E-03	N/A	1.0271	0.9965	0.9763	1.0526	-0.2050
Upright Limb	Average	1.36E-03	3.70E-03	1.018	1.003	0.979	1.041	0.198
Hinge	SLM 3	7.40E-04	2.88E-03	1.0281	1.0070	0.9649	1.0670	0.3503
Hinge	SLM 6	1.63E-03	4.28E-03	1.0247	1.0086	0.9667	1.0624	0.4550
Hinge	SLM 11	8.93E-04	N/A	1.0170	1.0010	0.9820	1.0365	0.1070
Hinge	SLM 12	8.86E-04	N/A	1.0157	1.0024	0.9819	1.0350	0.2157
Hinge	SLM 13	7.16E-04	N/A	1.0097	0.9999	0.9904	1.0200	0.0363
Hinge	SLM 18	7.51E-04	N/A	1.0164	0.9957	0.9880	1.0300	-0.4459
Hinge	SLM 19	1.05E-03	N/A	1.0290	1.0095	0.9622	1.0717	0.4460
Hinge	SLM 20	5.82E-04	N/A	1.0191	1.0024	0.9785	1.0421	0.1713
Hinge	SLM 21	1.15E-03	N/A	1.0237	0.9950	0.9814	1.0448	-0.3695
Hinge	Average	9.23E-04	3.58E-03	1.021	1.002	0.977	1.047	0.109
Overturned Limb	SLM 4	1.48E-03	4.03E-03	1.0211	1.0035	0.9755	1.0464	0.2714
Overturned Limb	SLM 5	1.63E-03	4.41E-03	1.0294	1.0026	0.9680	1.0640	0.1215
Overturned Limb	SLM 8	1.03E-03	4.70E-03	1.0232	0.9998	0.9770	1.0475	0.0060
Overturned Limb	SLM 9	7.69E-04	3.62E-03	1.0322	1.0078	0.9601	1.0775	0.3118
Overturned Limb	SLM 10	1.22E-03	3.41E-03	1.0346	1.0120	0.9570	1.0885	0.4586
Overturned Limb	SLM 17	1.37E-03	N/A	1.0187	1.0006	0.9806	1.0392	0.0567
Overturned Limb	LA	1.06E-04	N/A	1.02	1.00	0.98	1.04	-0.14
Overturned Limb	LC	1.14E-04	N/A	1.0164	1.001	0.9825	0.9685	-0.0162
Overturned Limb	LD	1.01E-04	N/A	1.0219	1.007	.9774	1.0461	0.0461
Overturned Limb	Average	8.49E-04	4.03E-03	1.023	1.002	0.975	1.041	0.109

Table 1: AMS parameters for sites collected during this study. κ30℃ is room temperature (≈30℃) bulk susceptibility; κ -197 ℃ is liquid nitrogen temperature (-197℃) bulk susceptibility; κMax, κInt and κMin are the three principal axes of susceptibility; P' is the degree of anisotropy [Jelinek, 1981; Hrouda, 1982]; and T is the anisotropy shape factor [Jelinek, 1981] (For equations see text).

9 Appendixes

9.1 Primary Data

Primary data collected in this study has been organized in Excel spreadsheets.

The BUSA MASTERSHEET.xlsx provides access to primary and analytical rock magnetic data.

AMS data is provided in the AMS Data_ALL.xls spreadsheet.

9.2 Anhysteretic Remanent Magnetization dataset

Early results of this study were based upon an ARM dataset which was found during spectral analysis to be inferior to the χ dataset. The ARM data series showed a much higher amplitude variability than χ especially in the conglomerate sections. The ARM dataset also had many more outliers which raised concerns about contamination of samples from clasts in the conglomerate. Therefore, the χ dataset was chosen for cyclostratigraphic analysis. However, the ARM data is still available as primary data and a robust red fit model [Mann and Lees, 1996] Appendix Figure 3 is presented.

Samples collected for χ analysis were also used in the ARM data series. Refer to Section 3.3 for sample collection and preparation details. ARM was applied with a decaying alternating field between 100-0 mT with a 97 μT DC biasing field and mass normalized. The ARMs were applied with a modified Schonstedt GSD-5 AC demagnetizer at Lehigh University.

ARM shows multi-hierarchical amplitude and frequency variability throughout the data series. Values range from 8.59×10^{-6} to 8.64×10^{-3} Am^2/kg, but some

of the highest values are $\gg 5\ \sigma$ from the mean value and have therefore been discarded; this relates to 6 samples or < 1 % of the total data and all of these samples are only present in the coarsest facies. The highest amplitude variations are also coincident with the coarsest facies. Power spectra obtained from MTM spectral analysis shows significant power in frequencies at both Milankovitch and non-Milankovitch scales, nearly all frequencies are significant (Appendix Figure 3). Tunes were attempted at short eccentricity (97-120 kyr), obliquity (41 kyr), and in the percessional index (16-24 kyr), but no tune was effective at isolating climate signals. Therefore, ARM was not used to create a robust cyclostratigraphy.

9.3 Appendix Figures

Appendix Figure 1: Correlation between published stratigraphic schemes of the region. This study uses a modified version of the Ford *et al.* [1997] formations and facies designations based on Barrier *et al.* [2010]. In this study we informally modified the formations in order to simplify recognition. A detailed description of the units used in this study can be found in Section 2.1 of this text.

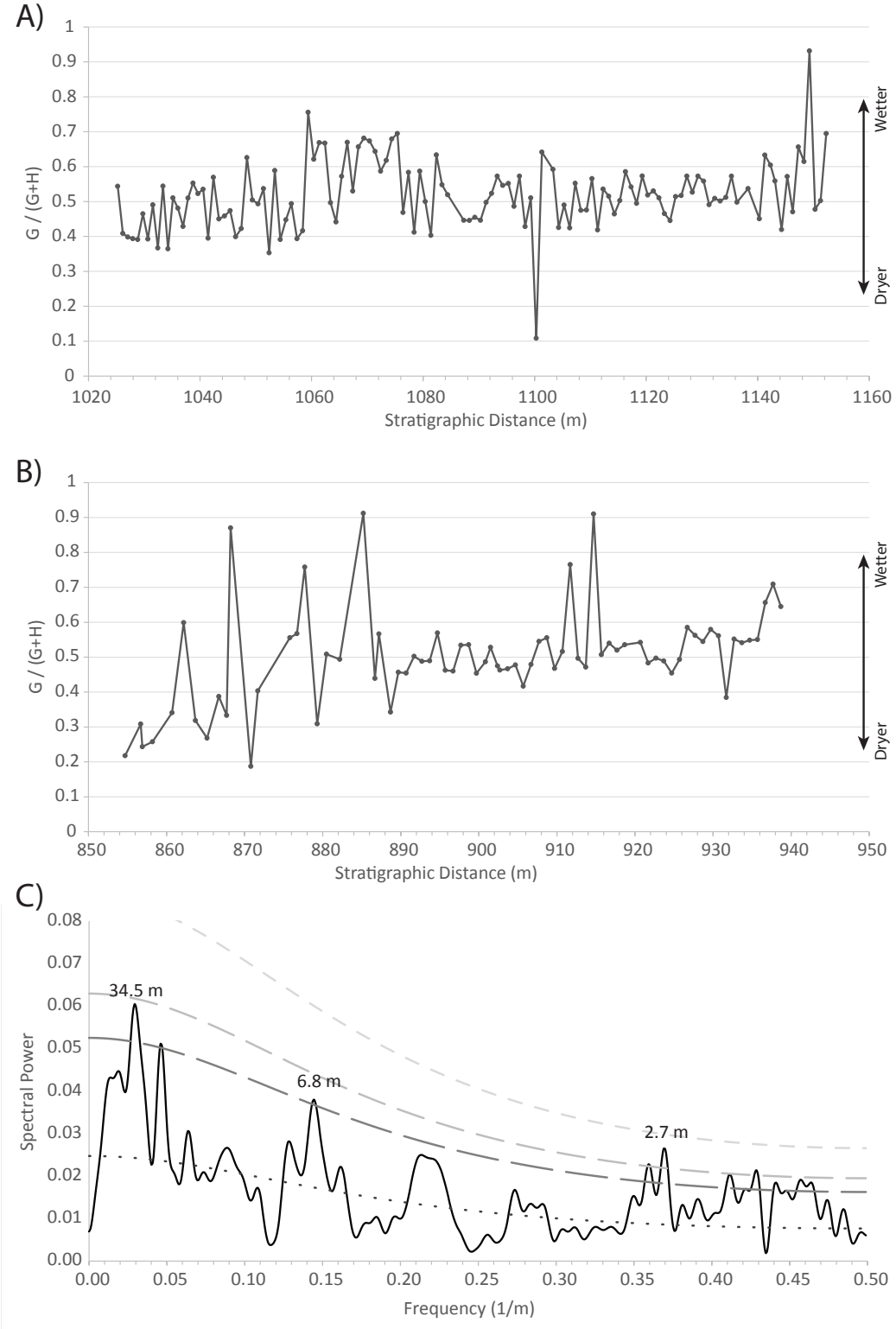

Appendix Figure 2: A) Goethite / Goethite + Hematite (G/ G + H) ratio for specimens from 1025 – 1152 m. B) G/ G + H ratio for specimens from 854 – 938 m C) Spectral analysis of A) with selected significant frequencies indicated. Solid curve is the power spectra, dotted line is the robust red noise model, and dashed lines are the 90, 95, and 99% confidence levels.

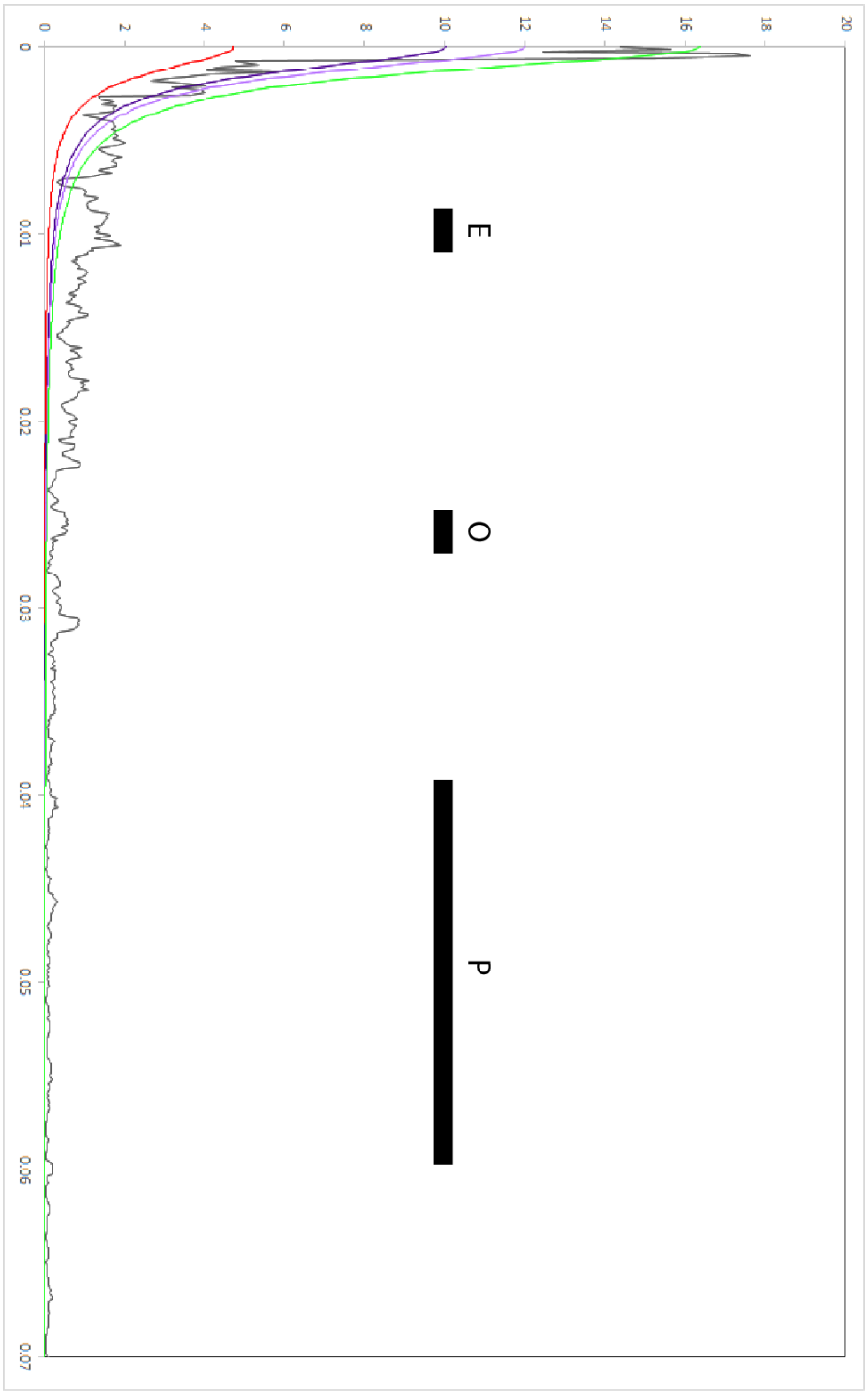

Appendix Figure 3: Un-tuned ARM spectra showing red noise (red), 90% (blue), 95% (purple), and 99% (green) confidence intervals. Expected orbital frequency extents are shown as black bars. Nearly all frequencies are significant at the 99 % confidence interval. For this reason the ARM was abandoned as a potential data set.

Appendix Figure 4: 1:200 scale stratigraphic column showing A) identified magnetozones, B) cyclostratigraphic sampling extent, C) unit formations, D) lithologic variations, and E) bedding variability

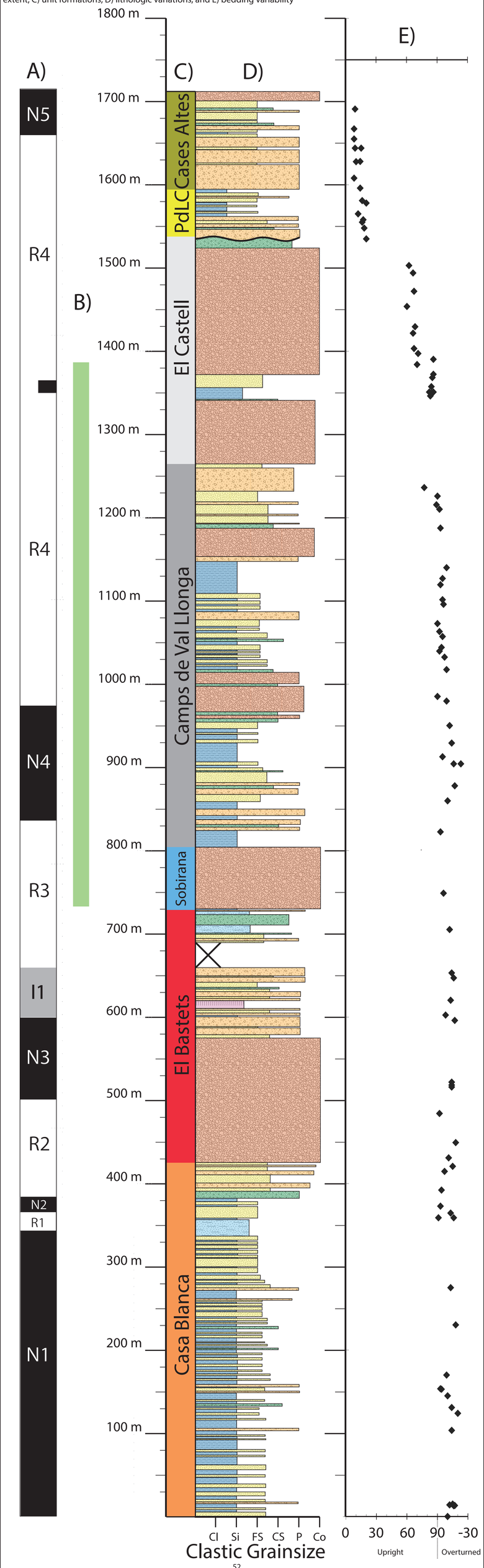

References Cited

Abdul Aziz, H., Hilgen, F., Krijgsman, W., Sanz, E., and Calvo, J. P. (2000). Astronomical forcing of sedimentary cycles in the middle to late Miocene continental Calatayud basin (NE Spain). *Earth and Planetary Science Letters*, 177:9–22.

Abrajevitch, A., Van der Voo, R., and Rea, D. K. (2009). Variations in relative abundances of goethite and hematite in bengal fan sediments: Climatic vs. diagenetic signals. *Marine Geology*, 267:191–206.

Allmendinger, R. W. (1998). Inverse and forward numerical modeling of trishear fault-propagation folds. *Tectonics*, 17(4):640–656.

Alonso, J. L., Colombo, F., and Riba, O. (2011). Folding Mechanisms in a Fault-propagation Fold Inferred from the Analysis of Unconformity Angles: The Sant Llorenc Growth Structure (Pyrenees, Spain).

Barberá, X., Cabera, L., Marzo, M., Parés, J. M., and Agustí, J. (2001). A complete terrestrial Olgiocene magnetobiostratigraphy from the Ebro Basin, Spain. *Earth and Planetary Science Letters*, 187:1–16.

Barrier, L., Proust, J.-N., Nalpas, T., Robin, C., and Guillocheau, F. (2010). Control of Alluvial Sedimentation at Foreland-Basin Active Margins: A Case Study from the Northeastern Ebro Basin (Southeastern Pyrenees, Spain). *Journal of Sedimentary Research*, 80:728–749.

Beausoleil, N., Lavallee, P., Yelon, A., Ballet, O., and Coey, J. (1983). Magnetic properties of biotite micas. *Journal of applied physics*, 54(2):906–915.

Borradaile, G. J. (1991). Correlation of strain with anisotropy of magnetic susceptibility (AMS). *Pure and Applied Geophysics*, 135(1):15–29.

Costa, E., Garcés, M., López-Blanco, M., Beamud, E., Gómez-Paccard, M., and Larrasoaña, J. C. (2010). Closing and continentalization of the South Pyrenean foreland basins(NE Spain): magnetochronological constraints. *Basin Research*, 22:904–917.

Egli, R. (2003). Analysis of the field dependence of remanent magnetization curves. *Journal of Geophysical Research: Solid Earth (1978–2012)*, 108(B2).

Erslev, E. A. (1991). Trishear fault-propagation folding. *Geology*, 19(6):617–620.

Fisher, R. (1953). Dispersion on a sphere. In *Proceedings of the Royal Society of London A: Mathematical, Physical and Engineering Sciences*, volume 217, pages 295–305. The Royal Society.

Ford, M., Williams, E. A., Artoni, A., Vergés, J., and Hardy, S. (1997). Progressive evolution of a fault-related fold pair from growth strata geometries, Sant Llorenç de Morunys, SE Pyrenees. *Journal of Structural Geology*, 19(96):413–441.

Ghil, M., Allen, M. R., Dettinger, M. D., Ide, K., Kondrashov, D., Mann, M. E., Robertson, A. W., Saunders, A., Tian, Y., Varadi, F., and Yiou, P. (2002). Advanced spectral methods for climate time series. *Reviews of Geophysics*, 40:3.1–3.41.

Gradstein, F. M., Ogg, J. G., Schmitz, M., and Ogg, G. (2012). *The Geologic Time Scale 2012 2-Volume Set*, volume 2. Elsevier.

Gunderson, K. L., Anastasio, D. J., Pazzaglia, F. J., and Picotti, V. (2013). Fault slip rate variability on 10^4-10^5yr timescales for the Salsomaggiore blind thrust fault, Northern Apennines, Italy. *Tectonophysics*, 608:356–365.

Gunderson, K. L., Pazzaglia, F. J., Picotti, V., Anastasio, D. A., Kodama, K. P., Rittenour, T., Frankel, K. F., Ponza, A., Berti, C., Negri, A., and Sabbatini, A. (2014). Unraveling tectonic and climatic controls on synorogenic growth strata (Northern Apennines, Italy). *Geological Society of America Bulletin*, 126(3):532–552.

Hardy, S. and Allmendinger, R. W. (2011). *Trishear: a review of kinematics, mechanics, and applications*. AAPG Special Volumes.

Hardy, S. and Ford, M. (1997). Numerical modeling of trishear fault propagation folding. *Tectonics*, 16(5):841–854.

Harris, S. E. and Mix, A. C. (2002). Climate and tectonic influence on continental erosion of tropical southe america, 0-13ma. *Geology*, 30(5):447–450.

Hinnov, L. A., Kodama, K. P., Anastasio, D. J., Elrick, M., and Latta, D. K. (2013). Global Milankovitch cycles recorded in rock magnetism of the shallow marine lower Cretaceous Cupido Formation, northeastern Mexico. *Geological Society, London, Special Publications*, 373(1):325–340.

Hrouda, F. (1982). Magnetic anisotropy of rocks and its application in geology and geophysics. *Geophysical surveys*, 5(1):37–82.

Jelinek, V. (1981). Characterization of the magnetic fabric of rocks. *Tectonophysics*, 79:T63–T67.

Jerolmack, D. J. and Paola, C. (2010). Shredding of environmental signals by sediment transport. *Geophysical Research Letters*, 37(July):1–6.

Kämp, N. and Schwertmann, U. (1983). Goethite and hematite in a climosequence in southern Brazil and their application in classification of kaolinitic soils. *Geoderma*, 29:27–39.

Kischvink, J. L. (1980). (the least-squares line and plane and the analysis of paleomagnetic data). *Geophysical Journal of the Royal Astronomial Society*, 62:699–718.

Kodama, K. and Hinnov, L. (2014). *Rock magnetic cyclostratigraphy*. John Wiley & Sons.

Kodama, K. P., Anastasio, D. J., Newton, M. L., Parés, J. M., and Hinnov, L. a. (2010). High-resolution rock magnetic cyclostratigraphy in an Eocene flysch, Spanish Pyrenees. *Geochemistry, Geophysics, Geosystems*, 11(June):1–22.

Kondrashov, D. and Ghil, M. (2007). Reply to T. Schneider's comment on "Spatio-temporal filling of missing points in geophysical data sets". *Nonlinear Processes in Geophysics*, 14:3–4.

Kruiver, P. P., Dekkers, M. J., and Heslop, D. (2001). Quantification of magnetic coercivity components by the analysis of acquisition curves of isothermal remanent magnetisation. *Earth and Planetary Science Letters*, 189:269–276.

Laskar, J., Robutel, P., Joutel, F., Gastineau, M., Correia, A., and Levrard, B. (2004). A long-term numerical solution for the insolation quantities of the Earth. *Astronomy & Astrophysics*, 428(1):261–285.

Latta, D. K., Anastasio, D. J., Hinnov, L. a., Elrick, M., and Kodama, K. P. (2006). Magnetic record of Milankovitch rhythms in lithologically noncyclic marine carbonates. *Geology*, 34:29–32.

Lowrie, W. (1990). Identification of ferromagnetic minerals in a rock by coercivity and unblocking temperature properties. *Geophysical Research Letters*, 17(2):159–162.

Mann, M. E. and Lees, J. M. (1996). Robust estimation of background noise and signal detection in climatic time series. *Climatic change*, 33:409–445.

Meyers, S. (2014). astrochron: An R Package for Astrochronology (Version 0.3.1).

Meyers, S. R., Sageman, B. B., and Hinnov, L. A. (2001). Integrated quantitative stratigraphy of the Cenomanian-Turonian Bridge Creek Limestone Member using evolutive harmonic analysis and stratigraphic modeling. *Journal of Sedimentary Research*, 71:628–644.

Mochales, T., Barnolas, a., Pueyo, E. L., Serra-Kiel, J., Casas, a. M., Samsó, J. M., Ramajo, J., and Sanjuán, J. (2012). Chronostratigraphy of the Boltaña Anticline and the Ainsa Basin (southern Pyrenees). *Bulletin of the Geological Society of America*, 124:1229–1250.

Nádor, A., Lantos, M., Tóth-Makk, A., and Thamó-Bozsó, E. (2003). Milankovitch-scale multi-proxy records from fluvial sediments of the last 2.6 Ma, Pannonian Basin, Hungary. *Quaternary Science Reviews*, 22:2157–2175.

O'Reilly, W. (1984). *Rock and mineral magnetism*. Springer.

Parés, J. M. (2004). How deformed are weakly deformed mudrocks? Insights from magnetic anisotropy. *Geological Society, London, Special Publications*, 238(1):191–203.

Parés, J. M. and van der Pluijm, B. A. (2002). Phyllosilicate fabric characterization by low-temperature anisotropy of magnetic susceptibility (LT-AMS). *Geophysical Research Letters*, 29(24):68–1.

Parés, J. M., van der Pluijm, B. A., and Dinarès-Turell, J. (1999). Evolution of magnetic fabrics during incipient deformation of mudrocks (Pyrenees, northern Spain). *Tectonophysics*, 307(1):1–14.

Puigfàbergas, C., Muñoz, J. A., and Vergés, J. (1992). Thrusting and foreland basin evolution in the Southern Pyrenees.

Rafini, S. and Mercier, E. (2002). Forward modelling of foreland basins progressive unconformities. *Sedimentary Geology*, 146:75–89.

Riba, O. (1967). Rsultados de un estudio sobre el Terciario continental de la parte este de la depresión central catalana. *Acta Geológica Hispànica*, 2:1–6.

Riba, O. (1976). Syntectonic unconformities of the Alto Cardener, Spainish Pyrenees: a genetic interpretation. *Sedimentary Geology*, 15:213–233.

Richter, C. and van der Pluijm, B. A. (1994). Separation of paramagnetic and ferrimagnetic susceptibilities using low temperature magnetic susceptibilities and comparison with high field methods. *Physics of the Earth and Planetary Interiors*, 82(2):113–123.

Rodríguez-Pintó, A., Pueyo, Emilio, L., Serra-Kiel, J., Samsó, J. M., Barnolas, A., and Pocoví, A. (2012). Lutetian magnetostratigraphy calibration of larger foraminifera zonation (SBZ) in the Southern Pyrenees: The Isuela section. *Palaeogeography Palaeoclimatology Palaeoecology*, 333–334:107–120.

Sangode, S. J. and Bloemendal, J. (2004). Pedogenic transformation of magnetic minerals in the Pliocene – Pleistocene palaeosols of the Siwalik Group, NW Himalaya, India. *Palaeogeography, Palaeoclimatology, Palaeoecology*, 212:95–118.

Sintubin, M. (1994). Clay fabrics in relation to the burial history of shales. *Sedimentology*, 41:1161–1169.

Solé-Sugrañes, L. (1972). Nota sobre una discordancia en el Eoceno medio del Perpirineo oriental. *Acta Geoloógica Hispánica*, 7:1–6.

Solé-Sugrañes, L. and Mascareñas, P. (1970). Sobre las formaciones Ager y Bagà, del Eoceno del Cadí (Perpirineo oriental) y de unos pretendidos olistolitos del mismo. *Acta Geoloógica Hispánica*, 4:97–101.

Soto, R., Larrasoaña, J. C., Arlegui, L. E., Beamud, E., Oliva-Urica, B., and Simón, J. L. (2009). Reliability of magnetic fabric of weekly deformed mudrocks as a paleostress indicator in compressive settings. *Journal of Structural Geology*, 31:512–522.

Suppe, J., Chou, G. T., and Hook, S. C. (1992). Rates of folding and faulting determined from growth strata.

Suppe, J., Sàbat, F., Anton Muñoz, J., Poblet, J., Roca, E., and Vergés, J. (1997). Bed-by-bed fold growth by kink-band migration: Sant llorenç de Morunys, eastern Pyrenees. *Journal of Structural GeologyJournal of Structural Geology*, 19(96):443–461.

Taberner, C., Dinarès-Turell, J., Giménez, J., and Docherty, C. (1999). Basin fill architecture and evolution from magnetostratigraphic cross-basin correlations in the southeastern Pyrenean foreland basin. *Geologic Society of America Bulletin*, 111:1155–1174.

Tarling, D. and Hrouda, F. (1993). *Magnetic anisotropy of rocks*. Springer Science & Business Media.

Tauxe, L. (2010). *Essentials of paleomagnetism*. Univ. of California Press.

Thomson, D. J. (1982). Spectrum estimation and harmonic analysis. *Proceedings of the IEEE*, 70:1055–1096.

Vergés, J., Fernàndez, M., and Martínez, A. (2002). The Pyrenean orogen: pre-, syn-, and post-collisional evolution. *Journal of the Virtual Explorer*, pages 55–74.

Williams, E. A., Ford, M., Vergés, J., and Artoni, A. (1998). Alluvial gravel sedimentation in a contractional growth fold setting, Sant Llorenc de Morunys, southestern Pyrenees. *Geological Society, London, Special Publications*, 134:69–106.

Yapp, C. (2001). Rusty relics of Earth History: Iron(III) oxides, isotopes, and surficial environments. *Annual Review of Earth and Planetary Sciences*, 29:165–199.

Zijderveld, J. D. A. (1967). Ac demagnetization of rocks: analysis of results. *Methods in paleomagnetism*, 3:254.

Vita

James Carrigan has broad interests in structural geology, especially related to how deformation is partitioned in contractional settings and the timescale which modulates orogenesis. He received a B.S. in Geology in 2013 from the University of Massachusetts Amherst.